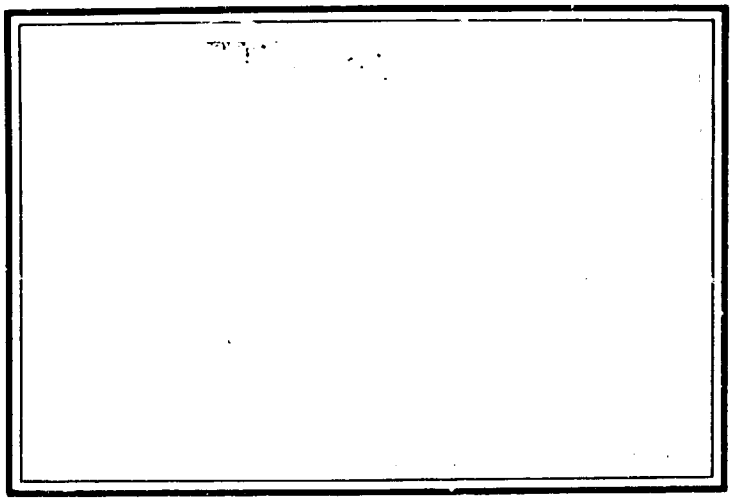

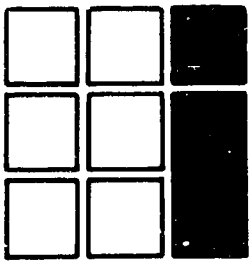

INTERMETRICS

EARTH RECOVERY MODE ANALYSIS FOR A MARTIAN SAMPLE RETURN MISSION

IR-287

Contract Number 955036

23 June 1978

Prepared for: Jet Propulsion Laboratory
4800 Oak Grove Drive
Pasadena, CA

Prepared by: J.P. Green
P.A. Grundy
C.M. Neily, Jr.
Intermetrics, Inc.
701 Concord Ave.
Cambridge, MA 02138

ACKNOWLEDGEMENTS

The work reported herein was performed for the NASA Jet Propulsion Laboratory under Contract No. 955036. Mr. Peter A. Grundy conducted the analyses presented in Sections 3,4,5 and Appendix A. Mr. John P. Green is responsible for Section 6; Mr. Clark M. Neily served as Project Manager and prepared the remainder of this report. The authors wish to gratefully recognize the efforts of Ms. Nancy L. Jenkins who produced the typescript, tables and figures.

TABLE OF CONTENTS

INTERMETRICS INCORPORATED · 701 CONCORD AVENUE · CAMBRIDGE MASSACHUSETTS 02138 · (617) 661-1840

TABLE OF CONTENTS (CON'T)

LIST OF FIGURES

LIST OF FIGURES (CON'T)

LIST OF TABLES

INTERMETRICS INCORPORATED · 701 CONCORD AVENUE · CAMBRIDGE, MASSACHUSETTS 02138 · (617) 661-1840

1.0 INTRODUCTION

This report summarizes work undertaken by Intermetrics in support of the JPL Mars Sample Return (MSR) mission feasibility evaluation. The analysis has concerned itself with evaluating alternative methods of recovering a sample module from a trans-earth trajectory originating in the vicinity of Mars. The major modes evaluated are:

(i) Direct atmospheric entry from trans-earth trajectory.

(ii) Earth orbit insertion by retro-propulsion.

(iii) Atmospheric braking to a capture orbit.

In addition, the question of guided vs. unguided entry vehicles has been considered, as well as alternate methods of recovery after orbit insertion for modes (ii) and (iii).

Chapter 2 presents a summary of results and conclusions reached in subsequent chapters. Chapters 3 and 4 discuss analytical results for aerodynamic and propulsive maneuvering vehicles respectively. Chapter 5 discusses system performance requirements, and Chapter 6 alternatives for inertial systems implementation. Chapter 8 discusses orbital recovery operations and Chapter 9 describes further studies required to resolve the recovery mode issue.

2.0 Summary and Conclusions

Based on the data presented in Chapters 5 and 6, all of the candidate methods appear to be technically feasible. The most severe system performance requirements are presented by low-angle, guided entry vehicles, and they apply primarily to the inertial subsystem initial alignment. Failure to achieve the required alignment accuracy, or significant degradation of the inertial subcomponents will cause large dispersions in impact point, and possibly loss of the sample module. Because an unguided vehicle does not depend on the correct operation of guidance, navigation, and control subsystems, it is not vulnerable to the class of failure modes arising out of the presence of such systems. For this reason, unguided aerodynamic vehicles are considered more reliable than guided, provided they can achieve the mission objectives. One such unguided vehicle is the high flight path angle, unguided ballistic entry body, which is the recommended approach to the minimum sample return mission.

Any vehicle targeted to enter or fly through any portion of the terrestrial atmosphere is vulnerable to on-board or ground system failures which prevent attainment of the required trajectory conditions or vehicle flight regime. If such failures occur prior to the time when the vehicle is first committed to an atmosphere encounter trajectory, the only result is loss of the sample module into interplanetary space. After committment to such an encounter trajectory, however, such failures must be considered as equivalent to compromise of the biologicalintegrity protocol associated with the recovery phase. Therefore the optimum recovery mode is considered to be one which does not require such targeting. This implies an earth orbit insetion by retro-propulsion followed by an orbital recovery system. It is suggested here that remote earth orbital operations, such as retrieval of objects above Space Shuttle operational altitudes, is likely to be a requirement shared by a community of users during the 1980's to 1990's time frame, and that development of

Shuttle compatible equipment should be undertaken. It is further suggested that return of the sample to a terrestrial laboratory can be accomplished by use of the Shuttle, provided that special measures are taken to ensure integrity of the sample container against an entry catastrophe.

Further studies are recommended to define structural, thermal protection, and weight characteristics of the "minimum" sample return module; to evaluate pre-deployment failure and trajectory control problems for the minimum mission; to develop earth encounter constraints for safe earth orbit injections for the optimium mission; and to assess the size and requirements of the community interested in remote earth orbital operations.

INTERMETRICS INCORPORATED • 701 CONCORD AVENUE • CAMBRIDGE, MASSACHUSETTS 02138 • (617) 661-1840

3.0 Aerodynamic Analysis

3.1 Introduction

Earth based retrieval of the Mars sample requires dissipation of the high kinetic energy acquired by the vehicle on the return orbit. A feasible approach to effecting this deceleration lies in exploiting the aerodynamic forces induced by motion of a vehicle through the Earth's atmosphere.

When the vehicle enters the atmosphere, it will experience drag, acting in direction opposite to the vehicle's motion, and possibly lift, acting normal to the direction of motion. These two forces, in combination with the Earth's gravitational attraction, centrifugal force, and the vehicle's inertia will completely condition the ensuing trajectory.

A vehicle encountering the atmosphere may slice through it and re-exit further along the path, or it may fall to the surface in a path wholly contained within the atmosphere. The occurrence of one or the other will depend on the vehicle's altitude rate at atmospheric encounter and the time history of altitude acceleration as governed by the radial component of the resultant of the above four operating forces on the vehicle.

For the re-exit trajectories, a critical consideration is the magnitude of the re-exit velocity. If the vehicle exits at hyperbolic speed, it will be lost into interplanetary space; at sub-parabolic exit speeds, the vehicle will be captured in an elliptic orbit around the earth. In the latter case the vehicle will re-enter the atmosphere in following orbital revolutions, suffering further deceleration and eventually falling to a landing in the earth's surface.

The above trajectory characteristics are defined by the vehicle's aerodynamic coefficients and the dynamic conditions at atmospheric encounter. For

given vehicle aerodynamic capabilities, ranges of initial conditions (entry corridors) can be defined which will yield corresponding terminal conditions: hyperbolic re-exit, re-exit to captured elliptical orbit (atmospheric braking), or direct fall to earth landing (direct entry).

When the returning vehicle encounters the atmosphere at orbital speeds, a shock wave will form ahead of the vehicle's nose, heating the local atmospheric section to very high temperatures. As the vehicle plunges deeper into a denser atmosphere, it will increasingly be heated by this enveloping layer, while the speed of the vehicle will continuously be reduced by the braking action of the atmosphere. In this fashion, a portion of the vehicle's kinetic energy is converted into heat.

The magnitude of the instantaneous deceleration applied to the vehicle, and the rate of heat flow to the body represent vehicle design parameters which must be met to insure vehicle survival during re-entry.

The operating drag deceleration varies directly with atmospheric density ρ and the square of vehicle velocity, v^2. As the path penetrates the atmosphere, the density increases rapidly, while velocity decreases due to the drag effect. The combination of these two countervailing effects causes a deceleration peak, with subsequent decreasing decelerations.

Heat rates into the vehicle, assuming a blunt nose design, result primarily from convective and radiative transfers from the shock layer. The operating rates, analagous to the vehicle deceleration, vary with atmospheric density and vehicle velocity, and exhibit a similar peak in their time histories. High heat rate trajectories are associated with high peak decelerations; however, the total heat flow into the body throughout the path tends to be smaller. That is, the high decelerations cause a rapid fall-off in vehicle velocity, and a consequent rapid reduction in the operating heat rates. The total heat flow, which reflects mainly this high, but short duration peak, is normally lower than for paths exhibiting lower peaks which subsist for longer time periods.

An important consideration in the design of any re-entry scheme is the sensitivity to errors, both in the nominal atmospheric encounter dynamic conditions and in the assumed vehicle and environment parameters. It is

particularly so in the case of hyperbolic return orbits because of the narrowness of the potential entry corridors, and the disastrous consequences of exceeding them. That is, on one side, hyperbolic re-exit and loss of the vehicle is possible; on the other, structural failure or burn-up of the vehicle in the atmosphere may result. Even if these extremes are avoided, significant dispersions in the final capture conditions may make eventual recovery of the sample difficult, if not impossible.

The above topics are analyzed in the following sections. Section 3.2 discusses the baseline Mars return orbits in terms of their implications for the atmospheric encounter problem, and identifies the main control parameters utilized in this study. Background material for this and following sections is presented in Appendix A in the form of an analysis of the equations of motion for a vehicle moving within the earth's atmosphere.

Section 3.3 discusses the direct entry capture mode. We first consider a ballistic vehicle and evaluate entry corridor, ranging capabilities, expected vehicle stresses, and error sensitivities. We then consider the effect of major modifications to the vehicle's capabilities, in particular, the addition of a lifting capability.

Section 3.4 considers the atmospheric braking capture mode. A similar format as the previous section is followed, with discussion of terminal conditions, vehicle stresses, and error sensitivities for a ballistic vehicle, and extensions to a lifting vehicle. Finally, we briefly discuss the decay characteristics of the established capture orbits.

3.2 Atmospheric Encounter Conditions

For a vehicle possessing a stable configuration at zero roll angle all operating forces (i.e., drag, lift, gravity, centrifugal) are contained in the plane defined by the vehicle's velocity and position-relative to earth-center vectors. The integration of the equations of motion in a wind-relative set of coordinate axes (see Appendix A) can then proceed from specification of the vehicle's earth relative velocity v and flight path angle δ at the atmospheric encounter altitude h.

For the Mars return hyperbolic orbits, the vehicle velocity and associated flight path angle, relative to a non-rotating earth, are given in terms of the orbit hyperbolic excess velocity v_∞ and the vacuum perigee radius r_p. The encounter azimuth Ψ_i cannot be so freely specified, but rather is constrained by the possible combinations of entry latitude L and orbital inclination i. The later is, furthermore, limited from below by the declination of the hyperbolic asymptote. However, the range of entry conditions can be investigated by arbitrarily assuming values of 0° (Ψ_i = -90°; L = 0°) and 180° (Ψ_i = 90°; L = 0°) for the inclination. The equations of motion involve, however, atmospheric airmass relative parameters, rather than inertial quantities. The two variable sets are related through Coriolis effects.

$$\underline{V} = \underline{V}_i - \underline{\Omega} \times \underline{r} \qquad (3\text{-}1)$$

where $\underline{\Omega}$ is the earth's angular velocity vector and $\underline{r}$ is the vehicle position vector with respect to the center of the earth.

Sample Mars return orbits, as described by the hyperbolic excess velocity vector $\underline{v}_\infty$, are given in Table 3-1.

Table 3-1: MSR Sample Orbits

	V_∞ (km/sec)	λ(deg)	δ(deg)
1	3.07	200.02	27.13
2	3.24	232.58	-52.45
3	2.82	314.52	-43.44

where λ is the right ascension and δ the declination. The corresponding atmospheric encounter velocities are given in Table 3-2.

Table 3-2: MSR Atmospheric Encounter Velocities

	v_i (kms/sec)	v_{max}(kms/sec)*	v_{min}(kms/sec)*
1	11.49216	11.7012	11.27927
2	11.53876	11.6823	11.39341
3	11.42793	11.5987	11.25453

*Note: for $\gamma_i = 0$

The first column represents encounter velocities relative to a non-rotating earth, the last two atmospheric airmass relative velocities for maximum and minimum relative speed encounters.

Thus, expected hyperbolic excess velocity variations do not significantly affect the atmospheric encounter speed. On the other hand, velocity dispersions at Mars departure are capable of producing significant changes in the orbit perigee altitude, and hence, in the atmospheric encounter flight path angle. This variable shall therefore constitute the control parameter for the following investigations of the atmospheric entry process, and will be utilized as the basis for definition of entry corridors for the considered vehicle capture modes.

The altitude at which aerodynamic flight is initiated is defined to be that of the outer edge of the earth's feasible atmosphere. This boundary is selected to be at an altitude above the earth's surface of 121.92 kms (400,000 ft), at which point the atmospheric density is of the order of 1.87×10^{-8} kgs/m^3.

3.3 Direct Entry

We are concerned here with the capture characteristics for direct atmospheric entry of unguided, fixed L/D vehicles. As discussed in Section 3.1, the parameters of concern are listed as

- entry corridor
- landing footprint
- maximum g-load
- maximum heat rate
- total heat load
- error sensitivities

Section 3.3.1 evaluates the above items for a ballistic vehicle, parameterized on the atmospheric encounter flight path angle and velocity. Section 3.3.2 considers the impact of changes in the vehicle's ballistic coefficient, and Section 3.3.3 discusses the effect of vehicle lifting capabilities.

3.3.1 Ballistic Vehicle

The baseline vehicle is a sphere of 1 meter radius, 30 kgs of mass, and ballistic coefficient B of .25 m^2/kg (i.e., $C_D = 2.4$).

Figure 3-1 presents plots of down-range in kms versus earth relative

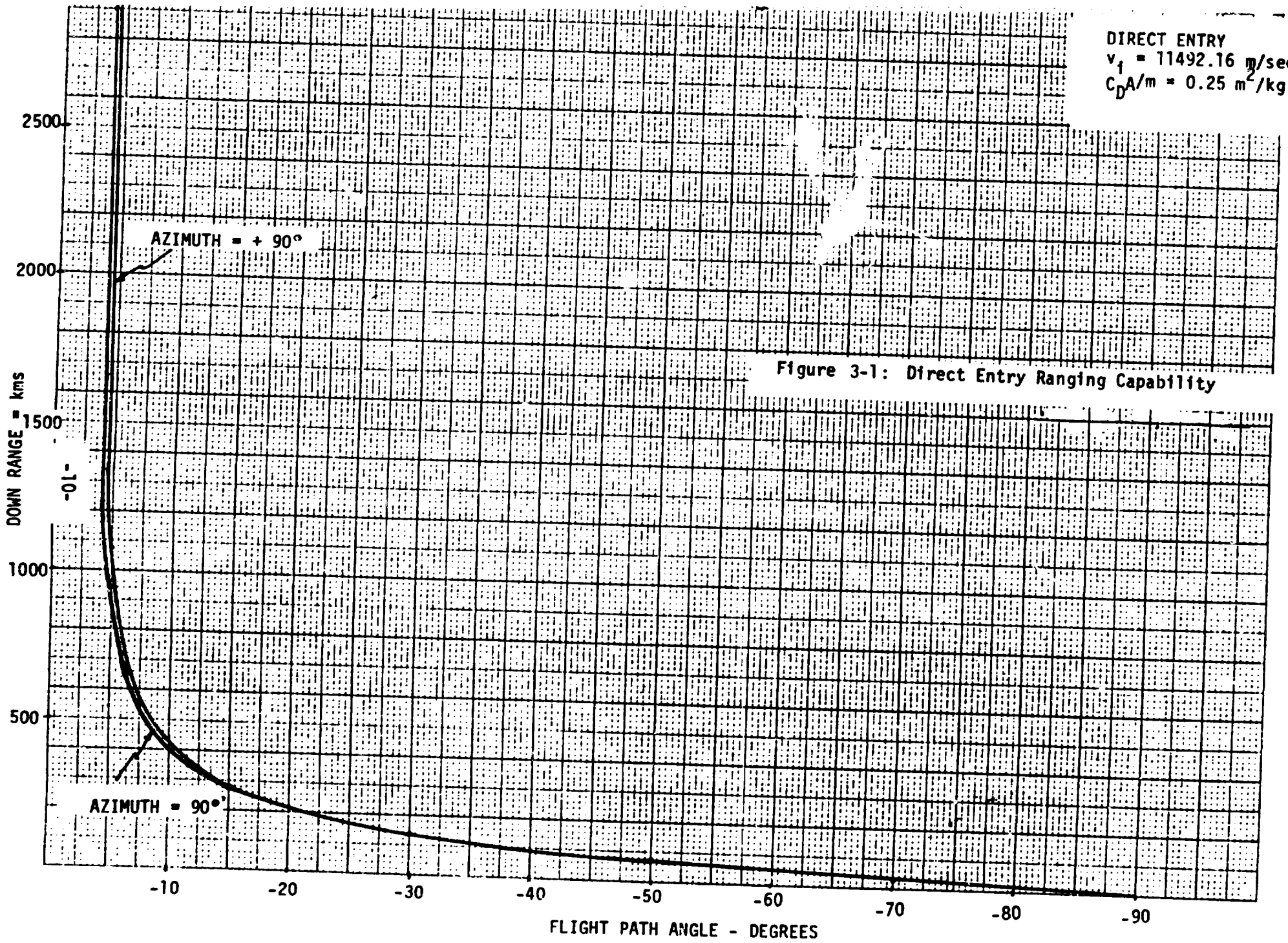

Figure 3-1: Direct Entry Ranging Capability

flight path angle in degrees. Curves are presented both for maximum and minimum earth relative velocity entry.

The plots are seen to rise steeply as the flight path angle approaches -4°. This unbounded rise indicates the presence of the overshoot boundary for the direct entry corridor - that is, at lower flight path angles, the vehicle does not fall to a landing, but rather re-exits from the atmosphere.

The overshoot boundary location is governed essentially by the vehicle's initial altitude rate; therefore, capture for maximum relative velocity entry is possible at shallower encounter flight path angles than for the minimum relative velocity case. Table 3-3 presents sample comparative values of achievable down-ranges.

The landing footprint, i.e., the range of reachable landing latitudes and longitudes, is determined by the downrange and the atmospheric encounter latitude, longitude and azimuth.

Due to the rotation of the earth, the encounter longitude is determined primarily by the vehicle time of arrival at the encounter altitude. The corresponding latitude and azimuth, however, cannot be so freely specified.

Specification of the return orbit vacuum perigee altitude (or equivalently, the encounter inertial flight path angle) fixes the angular deviation between the encounter radius and the direction of the hyperbolic excess velocity vector $\underline{v}_\infty$. Referring to Figure 3-2, the angle ν between the hyperbola's asymptote and the direction of the perigee radius is given by

$$\nu = \cos^{-1}(1/e) \tag{3-2}$$

where the eccentricity e is defined by

$$e = 1 + r_p/a$$

$$a = \mu/v_\infty{}^2 \tag{3-3}$$

while the polar angle f is given by

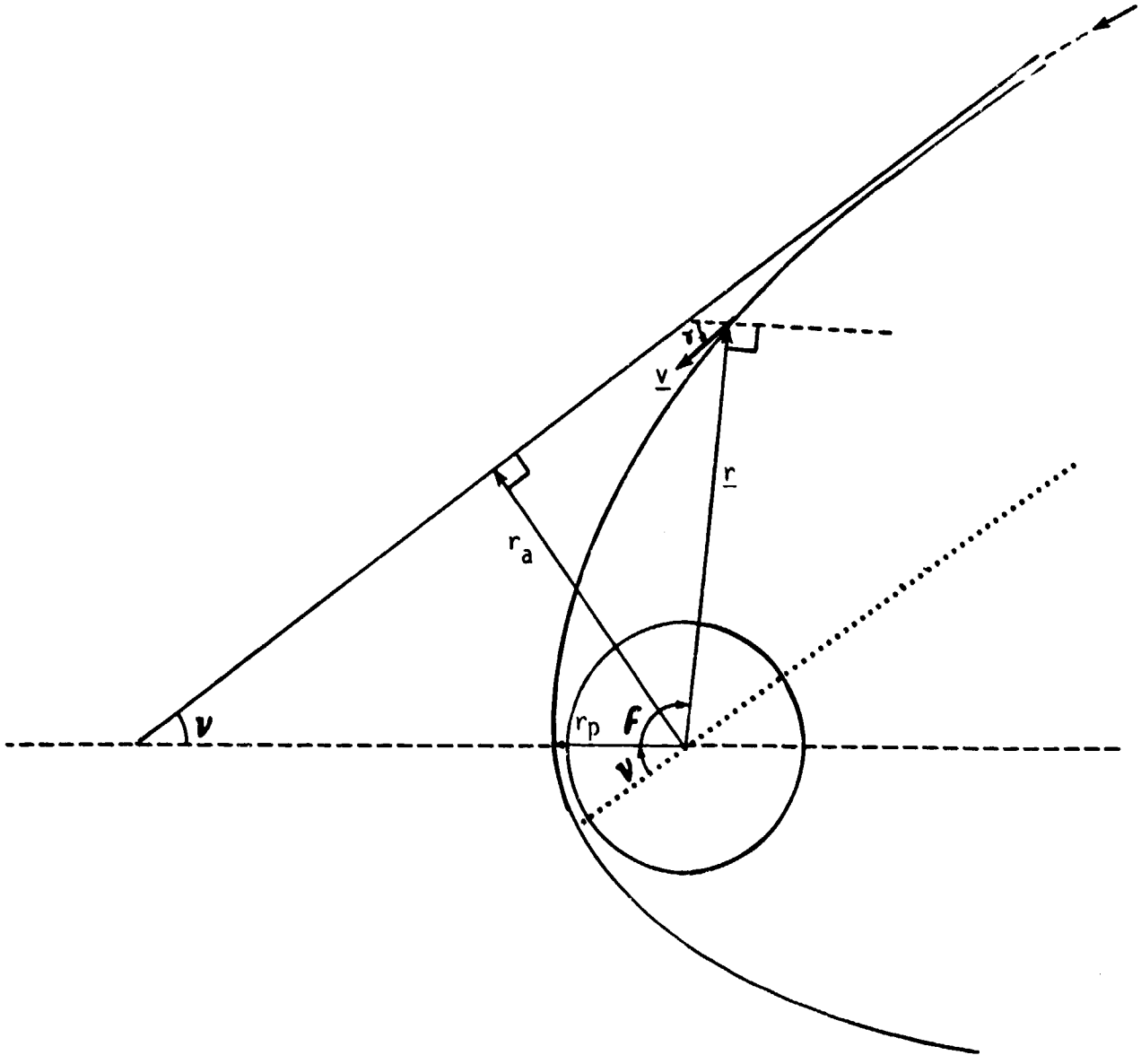

Figure 3-2: Hyperbolic Encounter Geometry

Table 3-3: Baseline Ballistic Vehicle Direct Entry Characteristics

Flight Path Angle-degrees	Down Range - kms		Time of Flight-secs		Max g-loading-g's		Max Heat Rate - Kcal/m^2/sec		Heat Load - Kcal/m^2	
	v_{max}	v_{min}	v_{max}	v_{min}	v_{max}	v_{min}	v_{max}	v_{min}	v_{max}	v_{min}
- 4	2895.4	-	2295	-	5.2	-	153.4	-	19620.5	-
- 4.4	-	6585.5	-	2848	-	4.7	-	122.8	-	18322.2
-5	944.7	1071.6	2050	2080	21.2	13.8	244.2	168.5	10420.1	9449.7
- 7.5	547.9	562.0	1990	2000	44.9	36.3	367.1	267.6	7587.5	6373.2
-15	273.0	274.3	1935	1939	95.7	80.8	569.9	410.1	5386.5	4397.0
-30	134.8	135.0	1890	1893	178.8	154.3	861.0	616.1	4106.6	3327.5
-50	68.0	68.1	1860	1862	270.6	237.2	1081.4	856.1	3443.4	2890.6
-70	29.8	29.9	1845	1846	319.5	309.1	1168.3	1048.1	3087.3	2798.0

INTERMETRICS INCORPORATED • 701 CONCORD AVENUE • CAMBRIDGE, MASSACHUSETTS 02138 • (617) 661-1840

$$f = \cos^{-1}[((r_p/r)(1+e) - 1)/e] \qquad (3\text{-}4)$$

The total angle $\Theta = f + \nu$ is therefore defined in terms of v_∞ and r_p (or γ_i) and is plotted in Figure 3-3 versus the encounter inertial flight path angle for the first return orbit listed in Table 3-1 (i.e., $v_\infty = 3.070$ kms/sec). The minor v_∞ variations for the remaining return trajectories listed in the table do not materially change the resulting Θ angle.

The angle Θ defines a cone of position about the hyperbolic excess velocity vector direction, with vertex at the earth center. The intersection of this cone with the earth-centered sphere of radius corresponding to the atmospheric encounter altitude is a circle, which constitutes the locus of atmospheric encounter points for a given flight path angle and hyperbolic excess velocity vector. In addition, all encounter points must be contained within a return orbital plane, which also includes the v_∞ vector. Based on these two geometric considerations, and utilizing standard spherical trigonometry relations, the entry latitude and inertial azimuth can be shown to satisfy

$$\sin L_e = \sin\delta \cos\Theta \pm \sin\Theta \sqrt{\sin^2 i - \sin^2\delta}$$

$$\sin\psi_i = -\cos i / \cos L_e \qquad (3\text{-}5)$$

where δ is the declination of the v_∞ vector and i is the inclination of the return orbital plane.

Note from the equations that, for inclination angles symmetric about 90° (i.e., i, 180°-i), the same entry latitude but antisymmetric entry azimuths are obtained. Furthermore, for any orbital inclination, two possible entry latitudes are obtained, corresponding to opposite directions of motion within the same orbital plane.

On the other hand, the motion of the vehicle within the atmosphere is constrained within an earth-fixed plane. The landing latitude is then given by

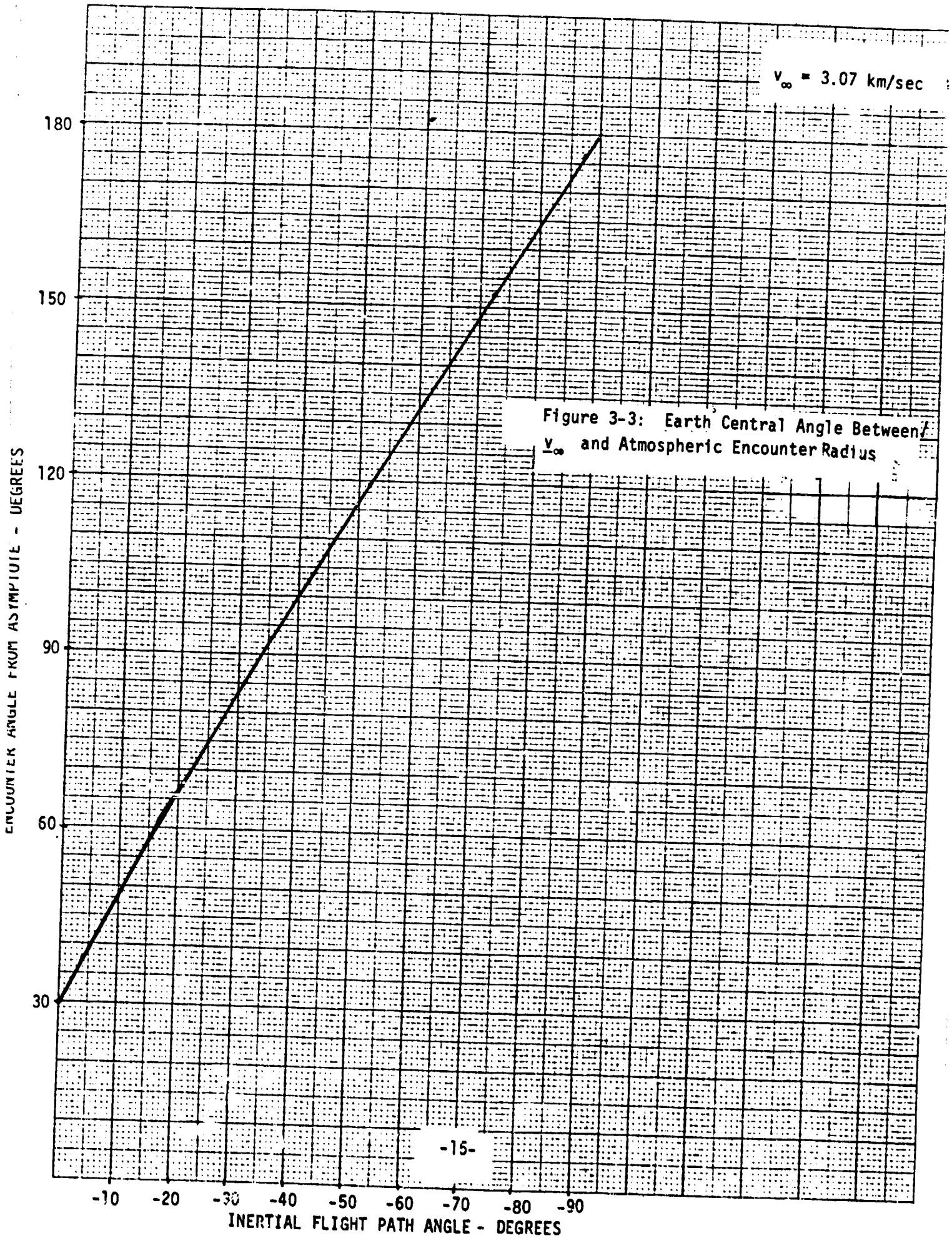

Figure 3-3: Earth Central Angle Between $\underline{V}_\infty$ and Atmospheric Encounter Radius

$$\sin L_\ell = \sin L_e \cos(R/r_e) + \cos L_e \sin(R/r_e)\cos\psi \qquad (3\text{-}5)$$

where R is the downrange and ψ is the earth-relative velocity-based azimuth angle.

The band of reachable landing latitudes is then determined by specification of $\underline{v}_\infty$, i, and γ_i. Figure 3-4 presents plots of landing point latitudes as a function of flight path angle for various orbital plane inclinations. The return trajectory represents the first case listed in Table 3-1, i.e., v_∞ = 3.07 km/sec, δ = 27.13°.

In the generation of these curves, the variation of achievable downrange with entry azimuth for a given flight path angle, was neglected. As shown in Figure 3-1, this effect is small for all encounter flight path angles not in the immediate vicinity of the overshoot boundary. In addition, the difference between inertial and relative encounter azimuth was also neglected. Again, this effect is not significant except in the immediate vicinity of the overshoot boundary.

Figure 3-5 presents the bounds of reachable latitudes for the two remaining return trajectories in Table 3-1, i.e., v_∞ = 3.24 km/sec, δ = -52.45° and v_∞ = 2.82 km/sec, δ = -43.44°. These bounds were obtained by solving for the landing point latitude for the 90° inclined orbit.

A characteristic of all direct entry paths considered is that they consist of a relatively brief period of deceleration followed by a similar equilibrium descent. That is, following the peak deceleration point, the vehicle is captured in a vertical air column, and descends in a regime where the drag deceleration is equal and opposite to gravity. The vehicle's velocity at any point is only a function of altitude, and is independent of initial encounter conditions.

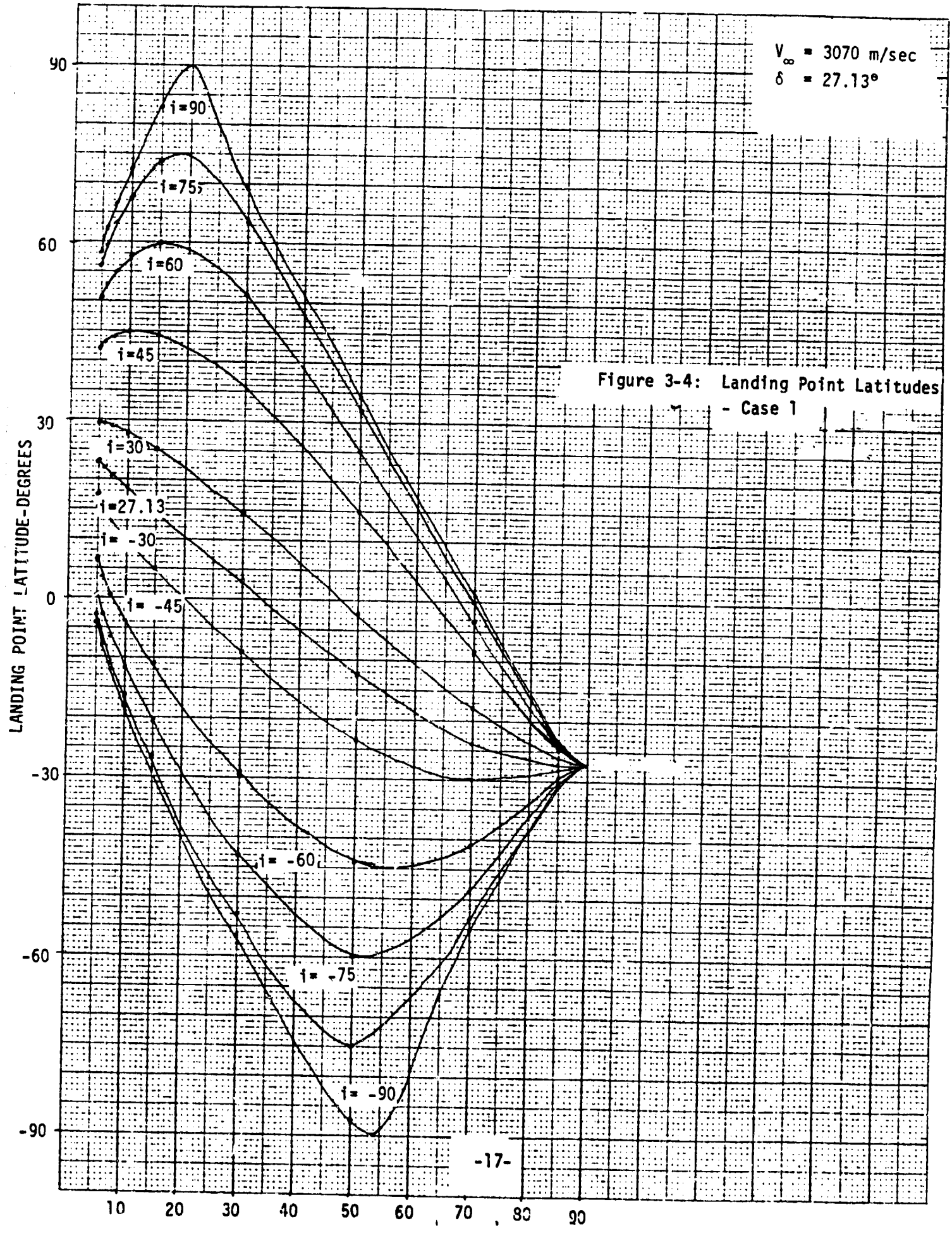

Figure 3-4: Landing Point Latitudes - Case 1

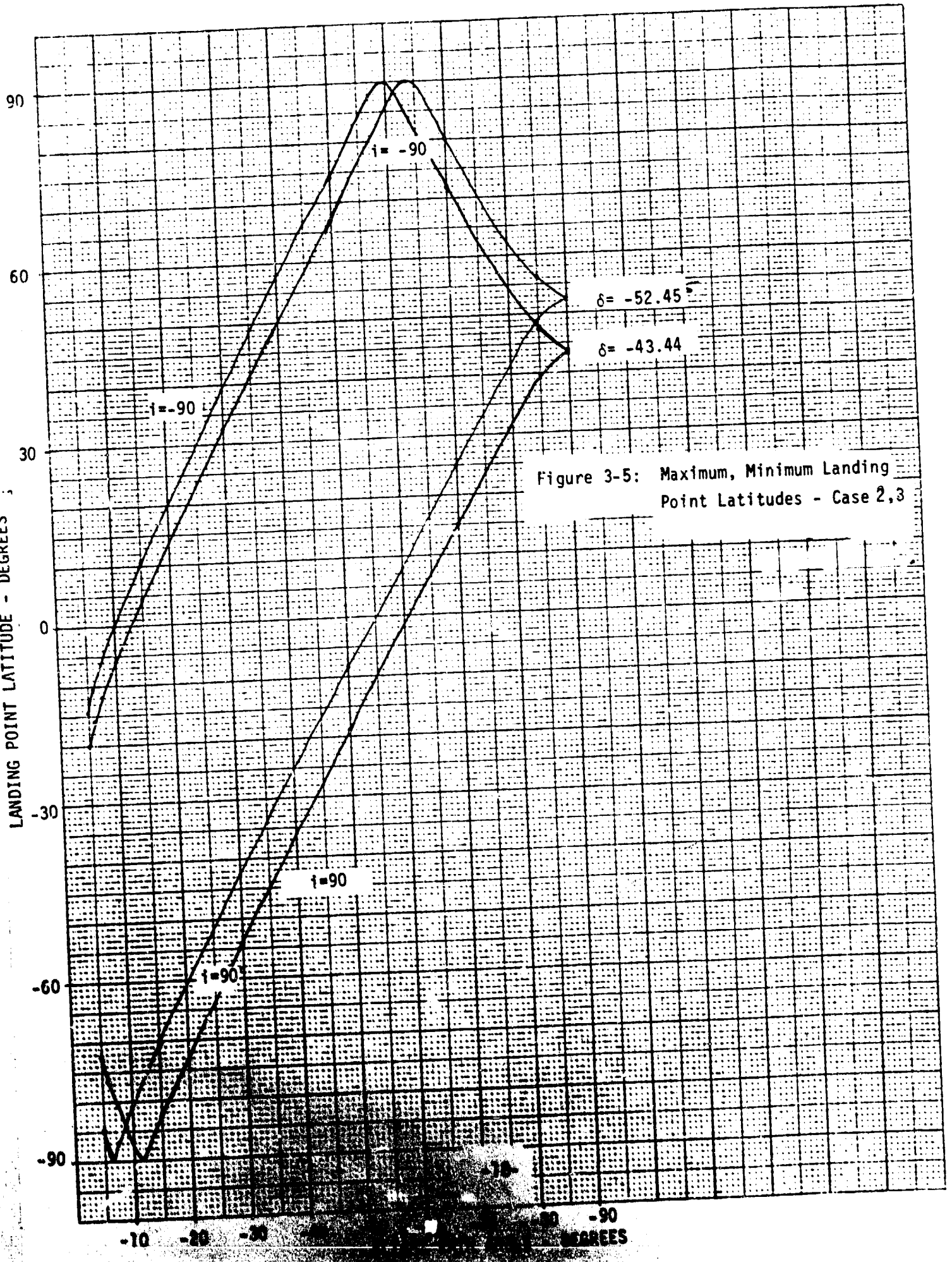

Figure 3-5: Maximum, Minimum Landing Point Latitudes - Case 2,3

The vehicle terminal velocity can be explicitly solved for in terms of surface atmospheric density and gravity magnitude, and is

$$v_f = 7.98 \text{ m/sec} \tag{3-7}$$

for the baseline vehicle. Furthermore, since most of the path is comprised by this equilibrium fall, the time-of-flight from atmospheric encounter to landing is relatively independent of encounter conditions. Sample values of this parameter are also listed in Table 3-3.

Figure 3-6 presents peak g-loading vs. encounter flight path angle curves for maximum and minimum relative velocity entry. The minimum peak loading for direct ballistic entry is seen to be on the order of 5 g's at the overshoot boundary, rising to 325 g's for vertical entry.

The maximum peak loading for maximum relative velocity entry does not occur at the earth relative flight path angle of -90°. Rather, it occurs at an inertial flight path angle of -90°, which, due to the motion of the earth, corresponds to a relative angle of about -87.5°. The relative angle of -90° is achieved at a slightly lower inertial angle on a positive heading, which results in partial cancellation of inertial velocity by earth speed, and therefore, a lower velocity of the vehicle relative to the air mass.

Figure 3-7 presents peak stagnation point heating rates and total heat load on the vehicle as a function of encounter flight path angle for maximum and minimum relative velocity entry. As shown, peak heating rates increase as the flight path angle tends towards -90°; however, as discussed in Section 3.1, total head loads on the vehicle decrease. The heating rate curve for maximum relative velocity entry exhibits, similarly to the g-loading curve, a maximum at an angle offset from -90°, and for the same reasons. Table 3-3 includes sample values of the above vehicle stress parameters for various encounter flight path angles.

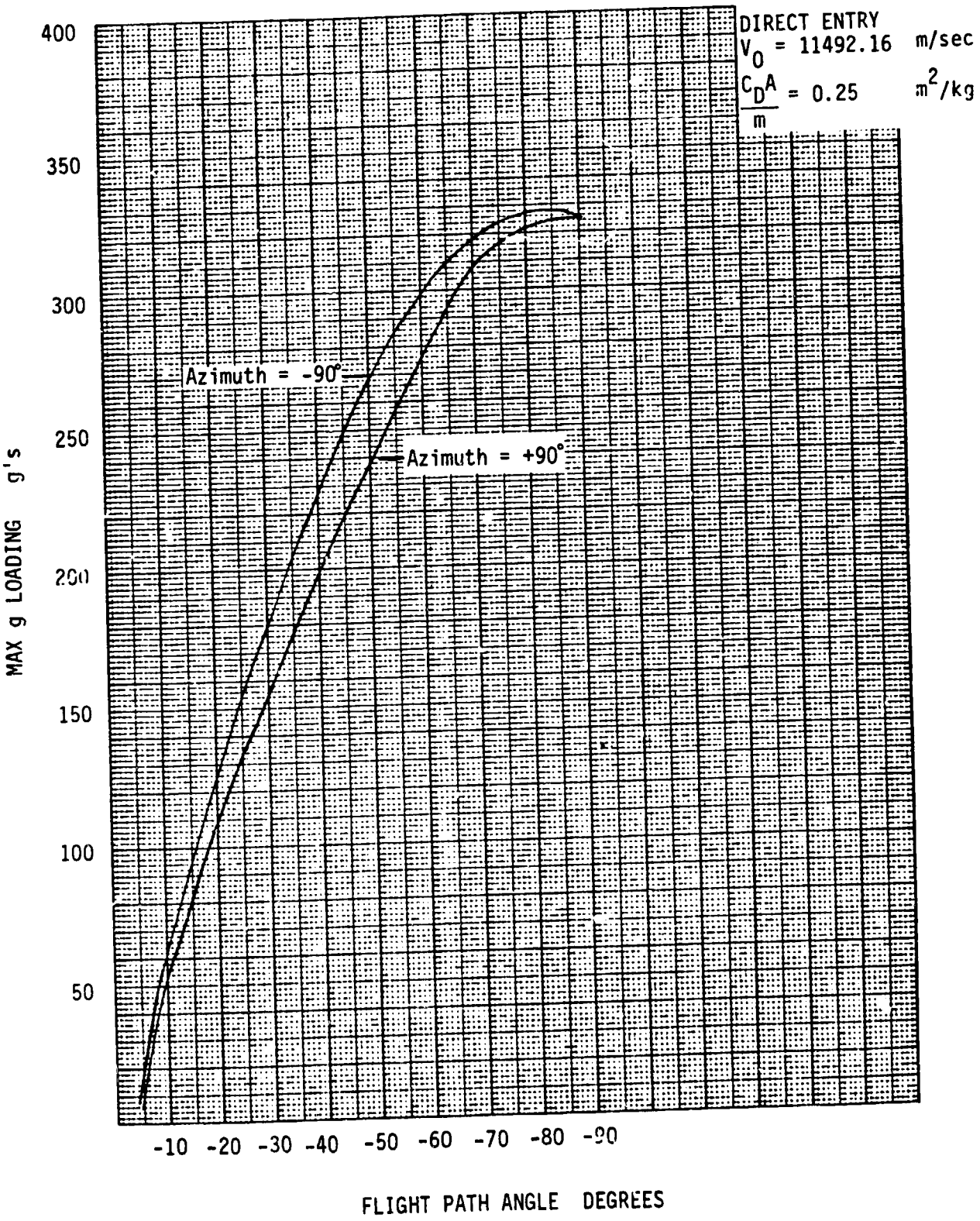

Figure 3-6: Maximum G-Loading - Direct Entry

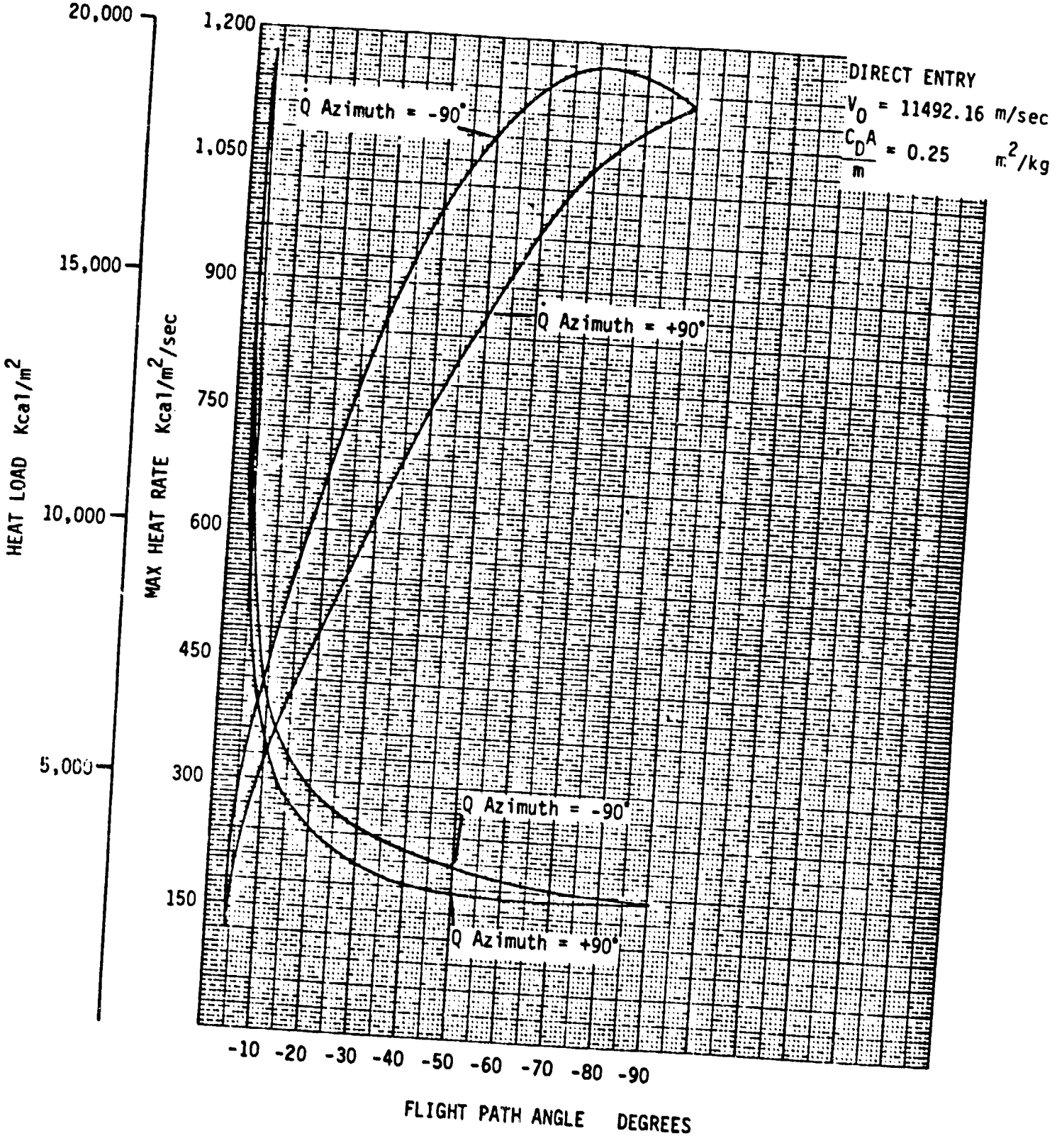

Figure 3-7: Maximum Heat Rates, Total Heat Load - Direct Entry

Figure 3-8 and Table 3-4 present down-range dispersion sensitivities to various error sources. Four driving errors are considered:

- error in assumed encounter velocity
- error in assumed encounter flight path angle
- error in assumed vehicle ballistic coefficient
- error in assumed atmospheric density profile

The provided curves represent the maximum relative velocity entry case. The similar performance exhibited in Figures 3-1, 3-6, and 3-7 by the maximum and minimum relative velocity entries indicates that similar qualitative behavior as shown in Figure 3-8 would be expected for the unrepresented cases.

The errors considered represent biases on the entry parameters. The ballistic coefficient error reflects uncertainties as to the vehicle's drag coefficient, reference area or mass. The atmospheric density error represents uncertainty in the density profile of a vertical air column; the formulated error is in the form of a percentage of the seasonal deformation ΔP of this profile, which tends to redistribute the air mass along the column.

The general shape of all four curves exhibits high sensitivities close to the overshoot boundary, which rapidly decay as the encounter flight path angle tends to -90°.

Specification of the most critical error source depends also on the definition of the level of expected driving errors. For normally expected values, it is clear that the encounter flight path angle represents the highest sensitivity error sources.

An alternative evaluation of these curves would lead to a specification of maximum allowable error source uncertainties for a specified level of acceptable down-range dispersions. Assuming uncorrelated error sources, the down-range error variance is given by

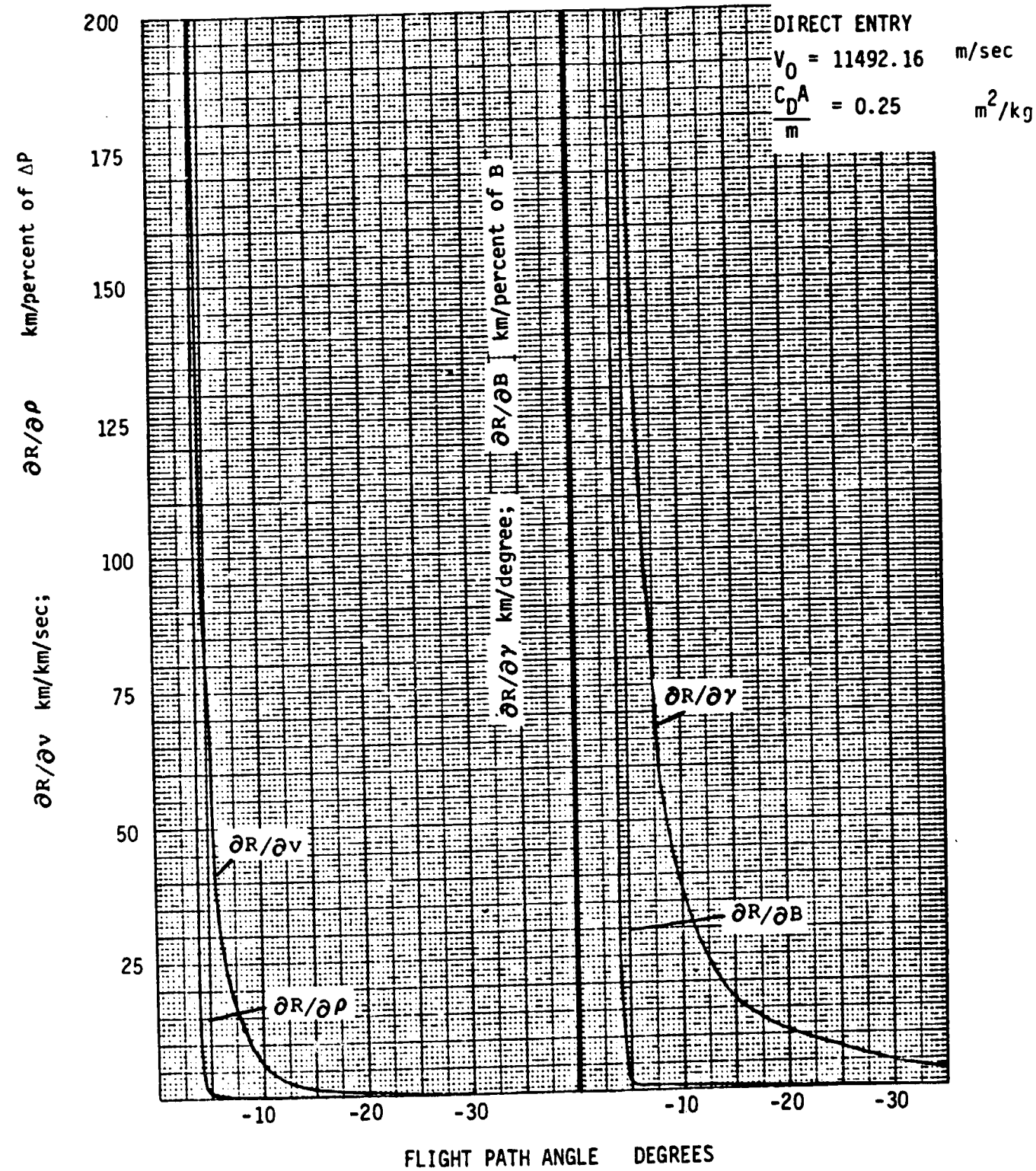

Figure 3-8: Down Range Error Sensitivities - Direct Entry

Table 3-4: Baseline Ballistic Vehicle Down-Range Error Sensitivities

Flight Path Angle-degrees	$\partial R/\partial v$-km/km/sec	$\partial R/\partial \gamma$-km/degree	$\partial R/\partial B$-km/percent of B	$\partial R/\partial \rho$-km/percent of $\Delta\rho$*
- 4	434.8	10273.6	-59.1	-14.4
- 5	94.4	314.7	- 1.7	- 0.75
- 7.5	16.8	76.3	- 0.7	- 0.3
-15	1.5	16.8	- 0.3	0
-30	0	4.9	0	0

*NOTE: $\Delta\rho$ = seasonal atmospheric density variation

INTERMETRICS INCORPORATED • 701 CONCORD AVENUE • CAMBRIDGE, MASSACHUSETTS 02138 • (617) 661-1840

$$\sigma_R^2 = (\partial R/\partial v)^2\sigma_v^2 + (\partial R/\partial \gamma)^2\sigma_\gamma^2 + (\partial R/\partial B)^2\sigma_B^2 + (\partial R/\partial \rho)^2\sigma_\rho^2 \qquad (3\text{-}8)$$

Assuming equal weights for all error sources, the acceptable uncertainty levels are given by

$$\begin{aligned} \sigma_v &= \sigma_R/2(\partial R/\partial v) \\ \sigma_\gamma &= \sigma_R/2(\partial R/\partial \gamma) \\ \sigma_B &= \sigma_R/2(\partial R/\partial B) \\ \sigma_\rho &= \sigma_R/2(\partial R/\partial \rho) \end{aligned} \qquad (3\text{-}9)$$

Given the down-range dispersion level (σ_R), these functions can readily be generated from the curves of Figure 3-8.

The figures and tables presented above provide a basis for evaluation of the viability of the direct ballistic atmospheric entry mode for capture of the returning Mars sample. Selection of acceptable entry trajectories is governed by

- maximum allowable vehicle stresses (g-loading, heating)
- desired landing footprint
- acceptable landing dispersions

Figures 3-6 and 3-7 allow translation of specifications of acceptable vehicle stresses into a range of permissible encounter flight path angles, and constrains the candidate values towards the horizontal or overshoot boundary. On the other hand, smaller flight path angles imply higher error sensitivities, and hence, higher landing point dispersions. For a given set of encounter condition uncertainties, constraints on acceptable landing dispersions will limit the range of permissible encounter flight path angles from below (i.e., constrains them towards the vertical), as shown in

Figure 3-8. Finally, the desired vehicle landing footprint must be matched with the set of reachable landing coordinates, as deduced from the vehicle ranging capabilities exhibited in Figure 3-2. This consideration will then define a third range of acceptable encounter conditions.

The desirable entry path is, therefore, one which is included in the three entry corridors defined above. If the intersection of these three sets is empty, then preservation of the direct entry mode will require at least one of the following

- modification of vehicle aerodynamic capabilities
- provision of guidance and control capabilities

The first item is discussed in the next two sections. The second is considered later in Chapter 5.

3.3.2 Ballistic Coefficient Effects

The ballistic vehicle aerodynamic characteristics are represented by the ballistic coefficient B. Figure 3-8 exhibits the effect (at least on down-range) of first order changes in this parameter. However, the strong non-linear character of the entry dynamics prevents extrapolation of these results to significant changes in B.

This section considers the impact of significant modifications to this parameter, resulting from changes in the vehicle drag coefficient, reference area or mass. In particular, we consider a reduction of the ballistic coefficient by a factor of four, i.e., a vehicle similar to the baseline but with a radius of .5 m, rather than 1m. Note that this modification implies an attendant reduction in the nose radius R_N utilized for heat transfer computations.

To provide insight into the effect, we exploit the approximate solutions given in Appendix A. We first consider the entry corridor definition. The direct entry overshoot boundary, for a ballistic vehicle, can be defined as that value of the encounter flight path angle for which the exit velocity is equal to the circular orbital velocity, i.e.,

$$v_E = \sqrt{gr_e} \tag{3-10}$$

The atmospheric braking undershoot boundary flight path angle can then be shown to satisfy

$$(r_e/h_s)(1 - \cos\gamma_o) = \sqrt{gr_e/v_o - 1} \tag{3-11}$$

and is independent of the ballistic coefficient. Therefore, within the limits of applicability of this approximate solution, changes to the vehicle ballistic coefficient have no impact on the entry corridor definition. That this solution is not totally sufficient in this region, however, is indicated by the fact that the resultant predicted exit flight path angle is the negative of the entry value which is clearly not the case, as the exit angle should tend to zero.

To assess the impact of ballistic coefficient changes on peak g-loading and heating rates, we can utilize the approximate solution in Appendix A for ballistic entry at medium and large flight path angles. The peak g-loading (see equation (A-24) does not contain any dependence on the ballistic coefficient. The terminal velocity, and therefore the impact shock, however, are affected. To preserve the drag-gravity equilibrium, changes in the ballistic coefficient are directly offset by changes in terminal velocity, such that the product B v_f^2 is constant.

The reduced coefficient vehicle terminal velocity is therefore

$$v_f = \sqrt{B^b/B}\ \ v_f^b \tag{3-12}$$

where the superscript b indicates values corresponding to the baseline vehicle.

The peak heating rate is (see equation (A-25)) dependent on the ballistic coefficient. A change in this parameter causes a corresponding change in the peak heating rate such that

$$\left(\frac{dQ_c}{dt}\right)_{max} = \sqrt{B^b\ R_N{}^b/B\ R_N}\ \ \left(\frac{dQ_c}{dt}\right)^b_{max} \tag{3-13}$$

Thus, in general, the character of the entry path is relatively insensitive to changes in the ballistic coefficient. To verify this assumption, numerical results have been generated for the reduced coefficient vehicle; the down-ranges are plotted for a shortened range of encounter flight path angles in Figure 3-9, and sample values of trajectory parameters are listed in Table 3-5 for the max relative velocity entry case. For comparison purposes, the down-range curve for the baseline vehicle is also included in the figure.

Comparison of Tables 3-3 and 3-5 shows, as expected, small changes in the peak g-load, and approximate doubling of peak heating rate and total heat load. Significant increases in the down-range and decreases in the time of flight relate to the higher vehicle velocity corresponding to any given value of drag deceleration. The down-range deviations, however, converge on the baseline vehicle values as the encounter flight path angle tends towards the vertical.

The similar shape of the down-range curves for the baseline and reduced ballistic coefficient vehicle imply that similar error sensitivities can be expected in the two cases. The major difference between the two curves

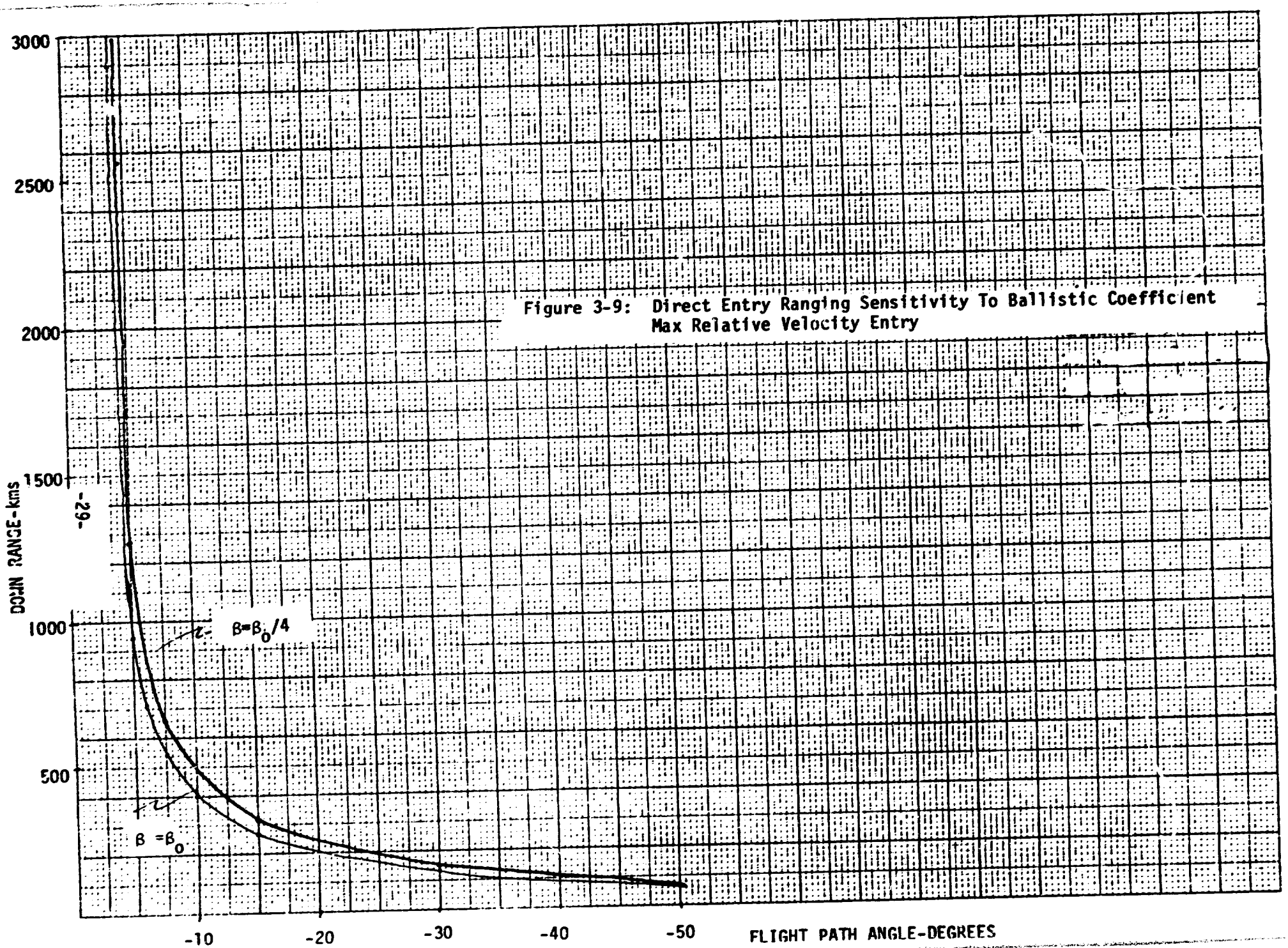

Figure 3-9: Direct Entry Ranging Sensitivity To Ballistic Coefficient
Max Relative Velocity Entry

Table 3-5: Reduced Coefficient Ballistic Vehicle Direct Entry Characteristics - Max Relative Velocity

Flight Path Angle-degrees	Down Range (kms)	Time-of-Flight (secs)	Max g-Loading (g's)	Max Heat Rate ($Kcal/m^2/sec$)	Heat Load ($Kcal/m^2$)
- 4.5	2562.7	1279	5.4	227.3	26290.8
- 5	1271.4	1116	13.5	312.75	17456.5
- 7.5	659.2	1030	36.4	512.9	12130.3
-15	316.3	966	83.9	882.2	8916.5
-30	152.9	920	165.3	1476.8	7211.6

INTERMETRICS INCORPORATED • 701 CONCORD AVENUE • CAMBRIDGE, MASSACHUSETTS 02138 • (617) 661-1840

corresponds to a shift of approximately 0.5° in the overshoot boundary of the applicable entry corridor.

3.3.3 Lifting Vehicle

The previous section exposed the relative insensitivity of the entry path to changes in the ballistic coefficient. A modification of the vehicle's aerodynamic characteristics that does significantly influence the entry trajectory, however, is the provision of a vehicle lift capability.

We consider here vehicle configurations which exhibit a constant L/D ratio in a stable, zero roll attitude, i.e., the lift vector is assumed to be always contained in the plane defined by the vehicle's position and velocity vectors, and to be normal to the velocity. The motion is then wholly contained within the same plane of ballistic entry.

Figure 3-10 plots downrange vs. encounter flight path angles for various vehicle L/D ratios. Comparison of these curves with Figure 3-1 points up two distinct effects of vehicle lift:

- The direct entry overshoot boundary is significantly shifted towards the vertical with increasing L/D
- Downrange sensitivities in the neighborhood of the overshoot boundaries decrease with increasing L/D, as evidenced by the slopes of the curves in that region

Figure 3-11 presents peak g-loadings on the vehicle for the same set of L/D ratios. The slope of the curves tends to decrease slightly with increasing L/D. A similar effect is evident in the operating heating rates on the vehicle.

The implication of the above results in that the addition of lift tends to desensitize performance in the neighborhood of the overshoot boundary, in that, for a specified ranging capability, smaller dispersions than for the ballistic entry case can be expected. Therefore, lifting vehicles will provide a wider range of permissible encounter conditions for which

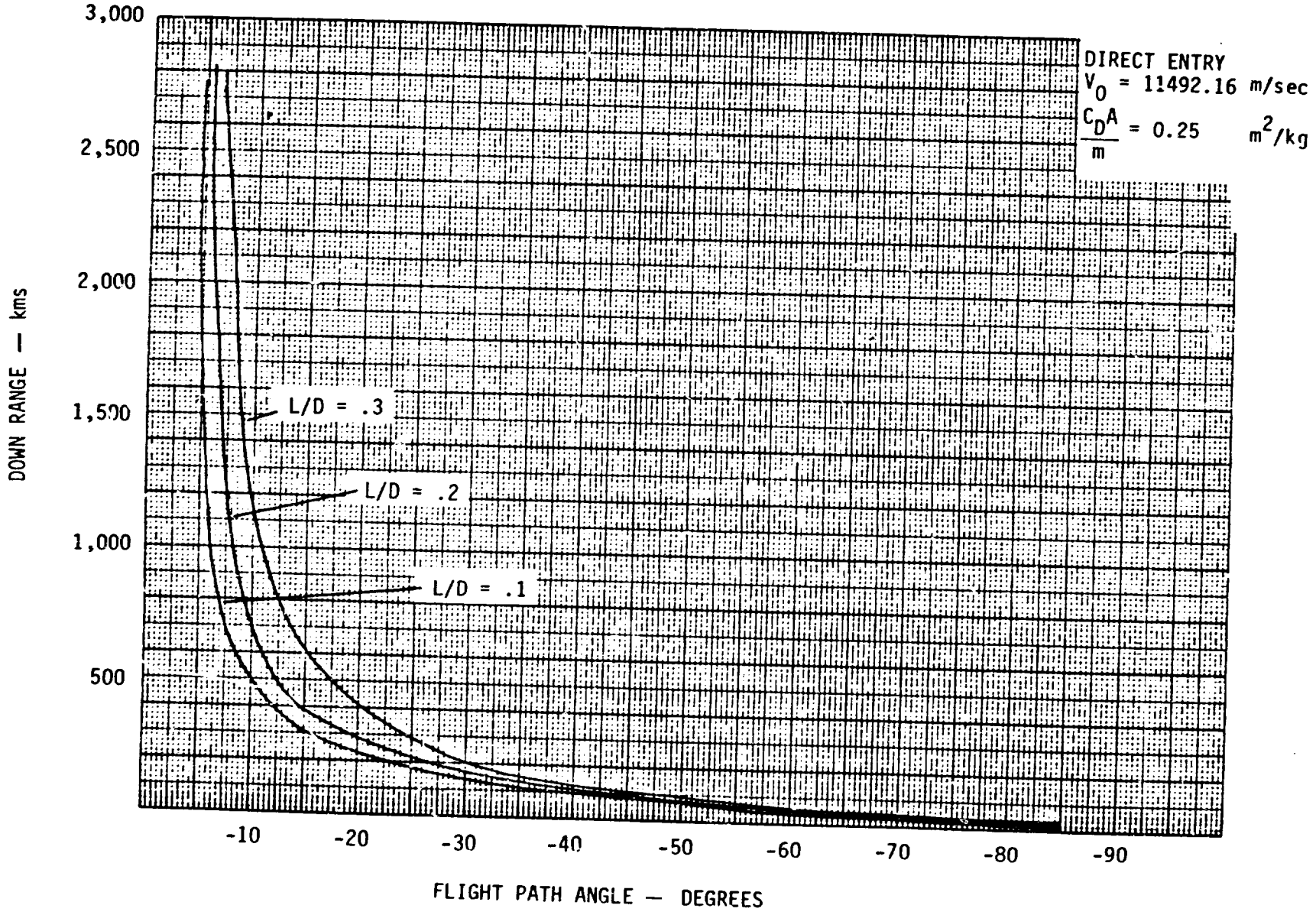

Figure 3-10: Down Range Sensitivity To Lifting Capability

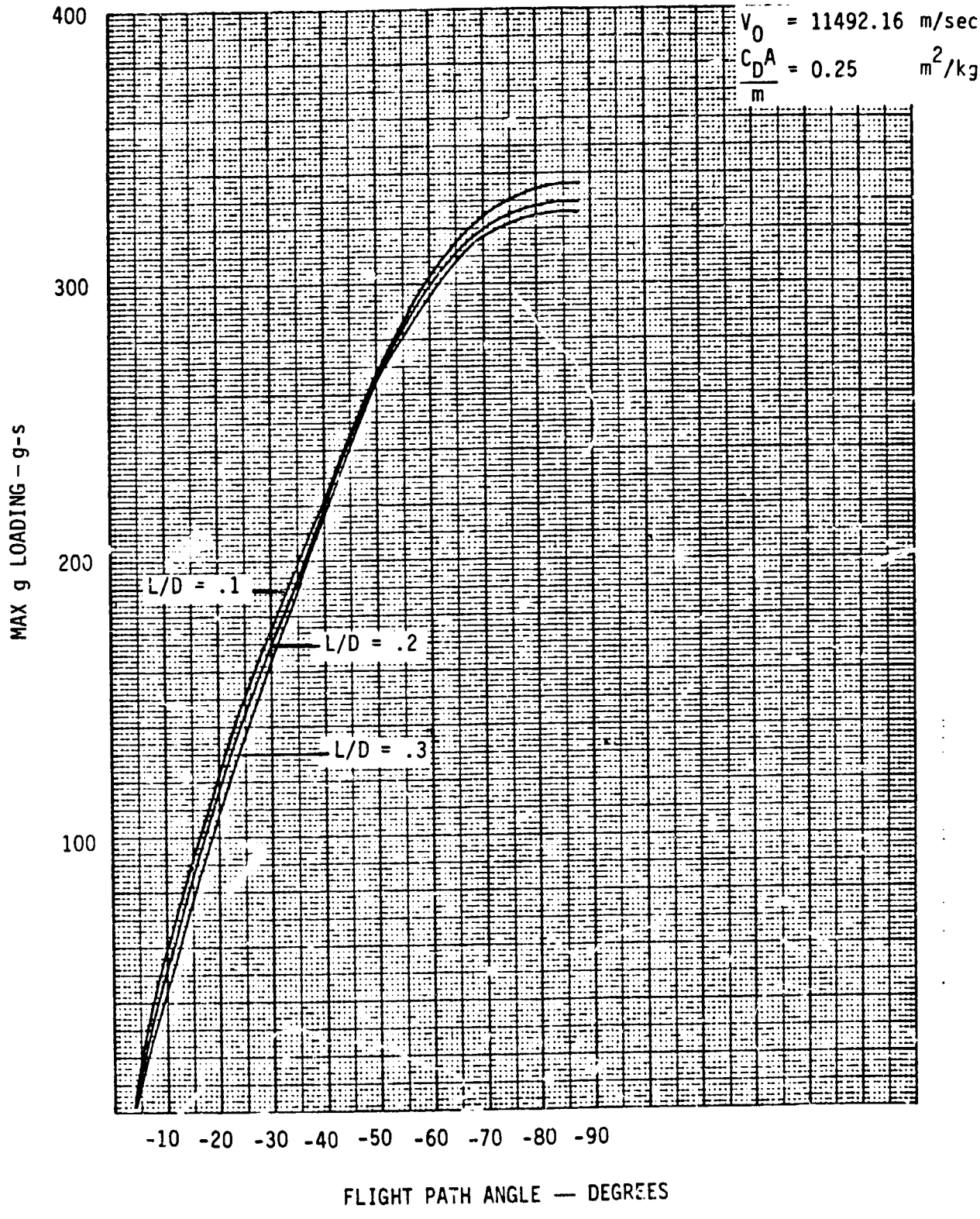

Figure 3-11: Maximum G-Loading For Lifting Vehicle - Direct Entry

acceptable landing dispersions can be achieved; i.e., the acceptable entry corridor is wider.

3.4 Atmospheric Braking

This section considers evaluation of entry corridor, capture characteristics, vehicle stresses and error sensitivities for the atmospheric braking maneuver, i.e., where the vehicle is passed through the atmosphere to dissipate part of its kinetic energy, yet retains sufficient velocity to re-exit into a captured elliptical orbit. Furthermore, since the perigee of the established orbit is within the atmosphere, the vehicle will (in the absence of a velocity increment) re-enter in subsequent resolutions, gradually dissipating more energy until it undergoes direct entry and lands. The gradual nature of the energy dissipation implies lower peak g-loadings and heating rates, so that this capture mode represents a conceptually attractive method from a vehicle stress viewpoint.

Section 3.4.1 considers the path characteristics for a ballistic, unguided vehicle. Section 3.4.2 assesses the impact of ballistic coefficient modifications, and Section 3.4.3 considers the lifting vehicle case.

3.4.1 Ballistic Vehicle

We consider here the baseline vehicle, with ballistic coefficient of .25 m^2/kg and zero L/D.

The entry corridor is limited from below by the condition of vehicle re-exit at still hyperbolic velocity, and consequent loss of the sample, and from above, by direct entry to a landing. The entry corridor is then given by that range of encounter flight path angles such that the exit velocity is subparabolic ($v_{ex}^2 < 2\mu/r_{at}$ - overshoot boundary), but supercircular ($v_{ex}^2 > \mu/r_{at}$ - undershoot boundary). Figure 3-12 plots inertial exit velocity versus encounter flight path angle for maximum and minimum earth relative velocity encounter. The acceptable encounter corridor is thus seen to be only on the order of 0.8° wide. Figure 3-13 presents the corresponding exit inertial flight path angle.

The two exit parameters determine the nature of the resulting orbits.

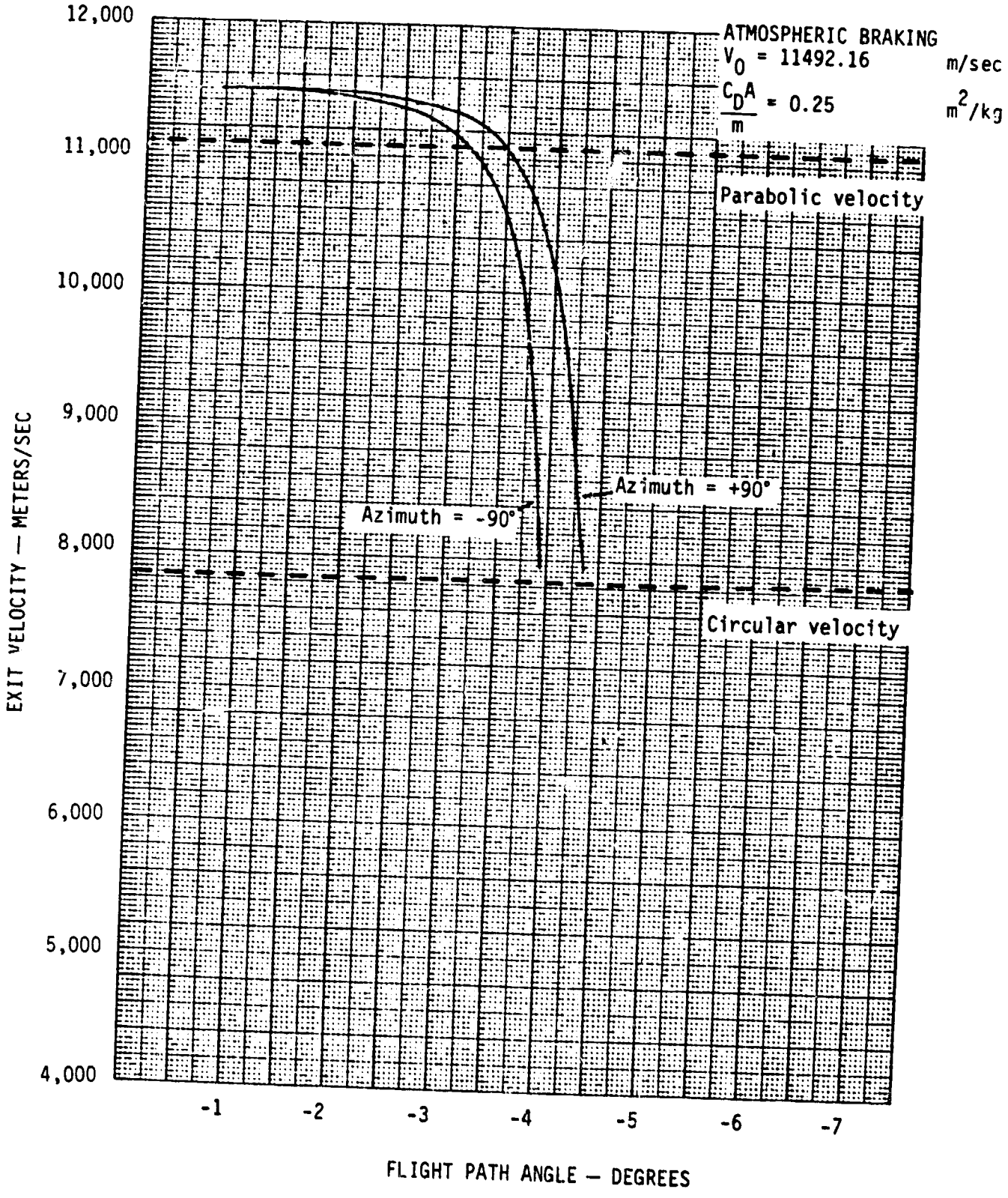

Figure 3-12: Inertial Exit Velocity - Atmospheric Braking

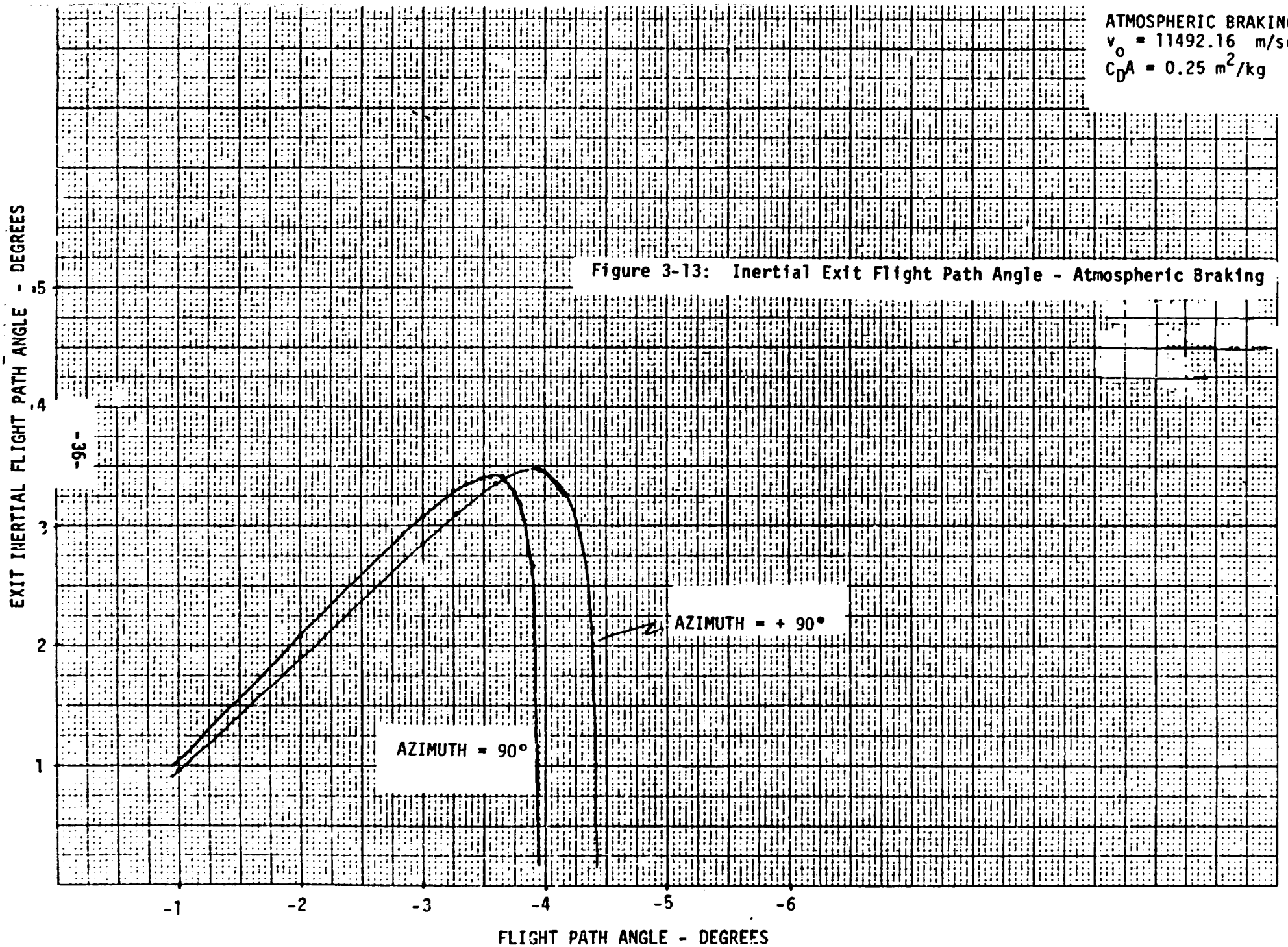

Figure 3-13: Inertial Exit Flight Path Angle - Atmospheric Braking

The corresponding perigee and apogee altitudes are given in Figure 3-14 as a function of the encounter flight path angle for the maximum relative velocity encounter case. Also included in the figure is the resulting orbital period, as given by

$$P = 2\pi\sqrt{a^3/\mu}$$
$$a = (r_p + r_a)/2 \qquad (3\text{-}14)$$

Table 3-6 presents sample values of peak g-loading, peak heating rate and total heat load encountered within the corridor for the maximum relative velocity encounter case.

Since the vehicle exits the atmosphere in an elliptical orbit with perigee within the atmosphere, it will re-enter on subsequent revolutions. Furthermore, the inertial re-encounter conditions are fixed by the previous exit conditions, i.e.,

$$v_{entry}^{n} = v_{exit}^{n-1}$$
$$\gamma_{entry}^{n} = -\gamma_{exit}^{n-1} \qquad (3\text{-}15)$$

Subsequent passes through the atmosphere result in either a direct entry to landing, or a reshaping of the orbit in terms of a reduction in the perigee and apogee altitudes. Figure 3-15 presents the changes in perigee and apogee altitudes of subsequent revolutions relative to the parameters of the initial orbit, as a function of the initial encounter flight path angle.

Figure 3-12 exhibits the narrowness of the entry corridor and steepness of exit velocity vs. encounter flight path angle curves. It may be expected from this, that high error sensitivities will be encountered for this maneuver. Figure 3-16 presents the error partials of exit velocity to errors in initial encounter velocity and flight path angle, vehicle ballistic coefficient and atmospheric density. Figure 3-17 presents the corresponding

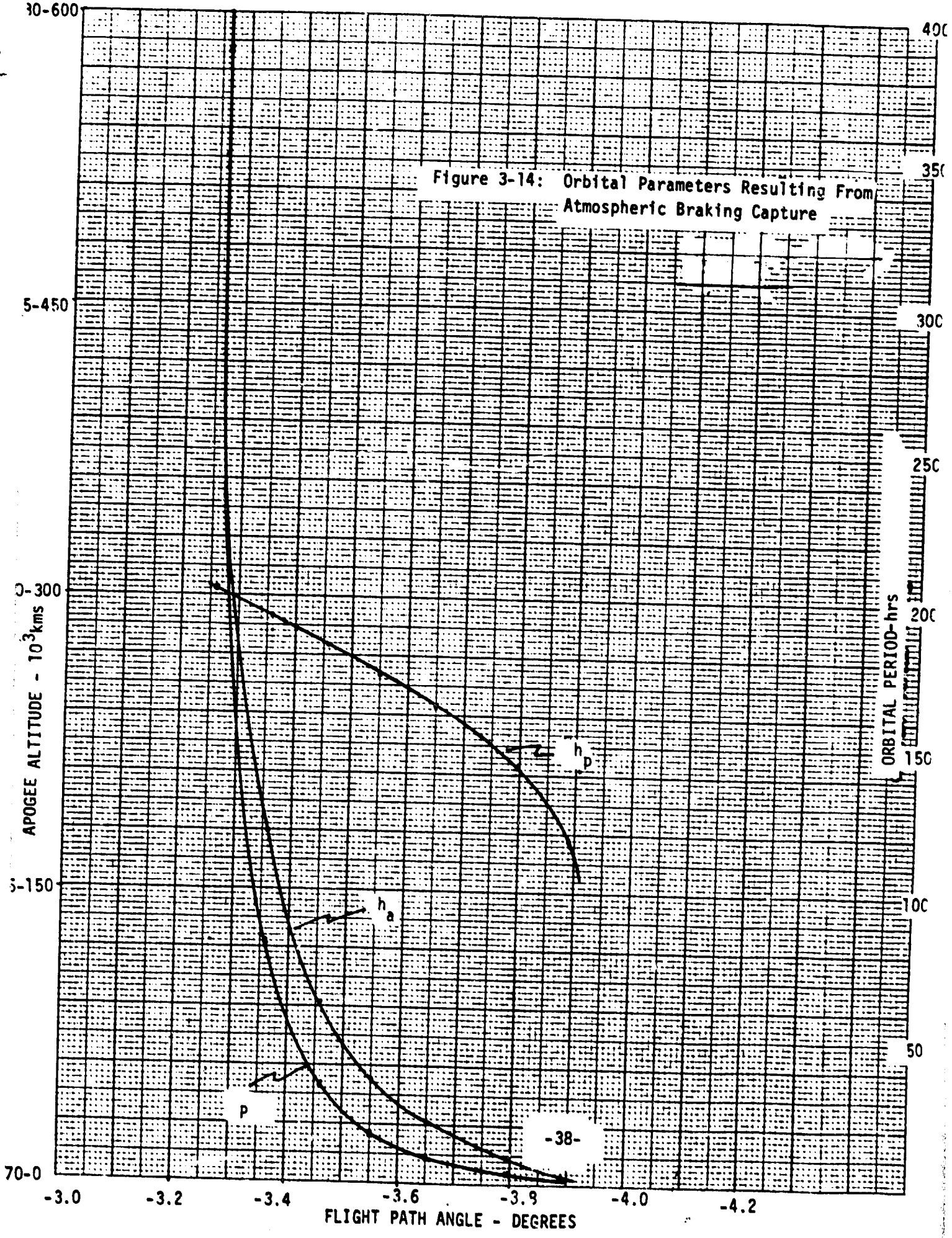

Figure 3-14: Orbital Parameters Resulting From Atmospheric Braking Capture

Table 3-6: Baseline Ballistic Vehicle Atmospheric Braking Characteristics - Max Relative Velocity

Flight Path Angle-degrees (γ_i)	v_{EXIT} Inertial (kms/sec)	γ_{EXIT} Inertial (degrees)	Time-of-Flight (secs)	Max g-Loading (g's)	Max Heat Rate (Kcals/m^2/sec)	Heat Load (Kcals/m^2)
-3.27 (-3.4)	11.0	3.29	131	.81	72.4	5926.5
-3.46 (-3.6)	10.73	3.39	143	1.26	88.5	7432.1
-3.65 (-3.8)	10.23	3.39	159	2.03	108.5	9417.2
-3.75 (-3.9)	9.82	3.29	172	2.6	120.0	10673.2
-3.89 (-4.05)	8.78	2.67	212	3.85	138.6	13131.1

INTERMETRICS INCORPORATED • 701 CONCORD AVENUE • CAMBRIDGE, MASSACHUSETTS 02138 • (617) 661-1840

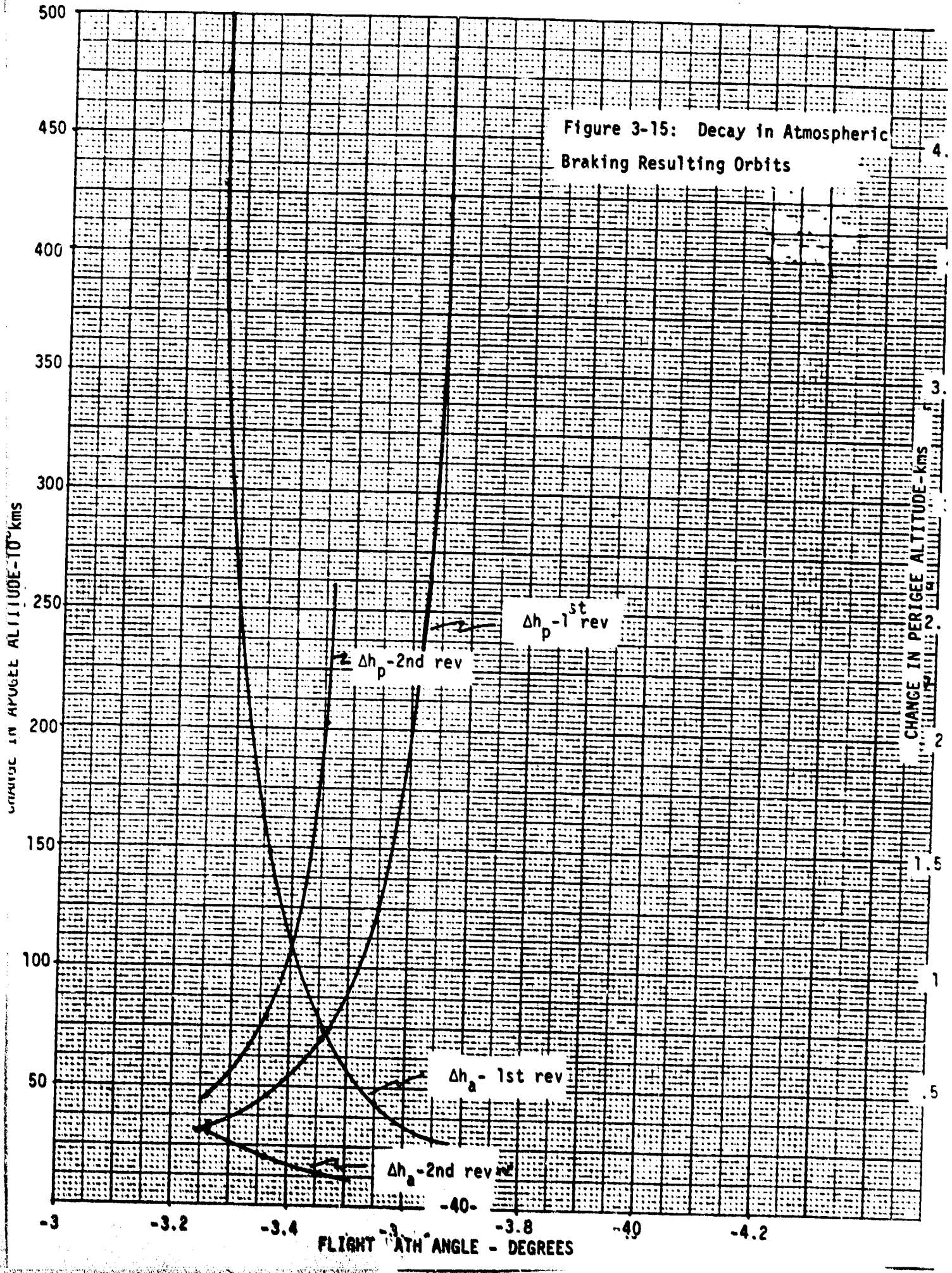
Figure 3-15: Decay in Atmospheric Braking Resulting Orbits
CHANGE IN APOGEE ALTITUDE-10³kms
CHANGE IN PERIGEE ALTITUDE-kms
FLIGHT PATH ANGLE - DEGREES
Δh_p-1st rev
Δh_p-2nd rev
Δh_a- 1st rev
Δh_a-2nd rev
500
450
400
350
300
250
200
150
100
50
-3
-3.2
-3.4
-3.8
-40
-4.2
4.
3.
2.
1.5
1
.5

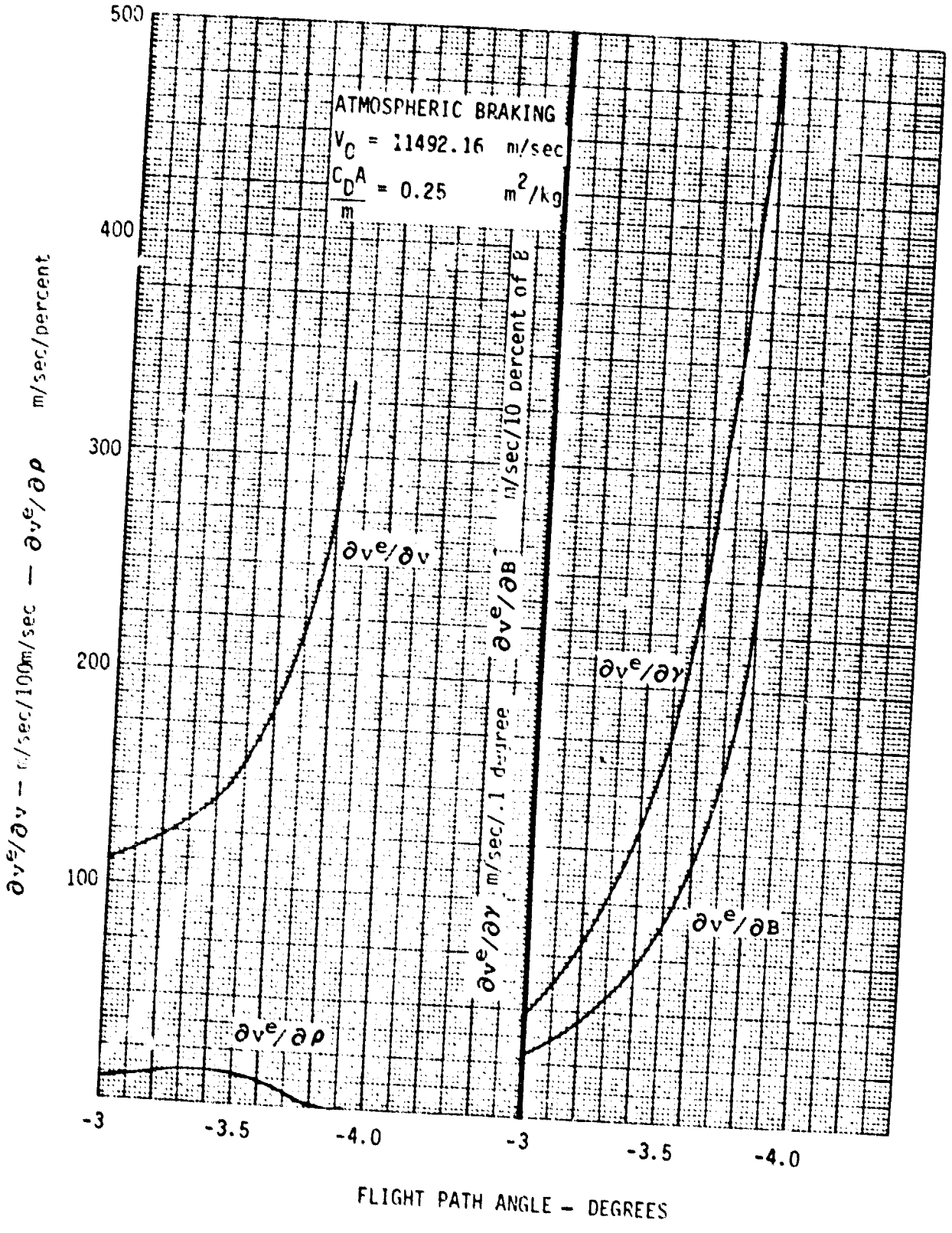

Figure 3-16: Exit Velocity Sensitivities - Atmospheric Braking

Figure 3-17: Exit Inertial Flight Path Angle Error Sensitivities

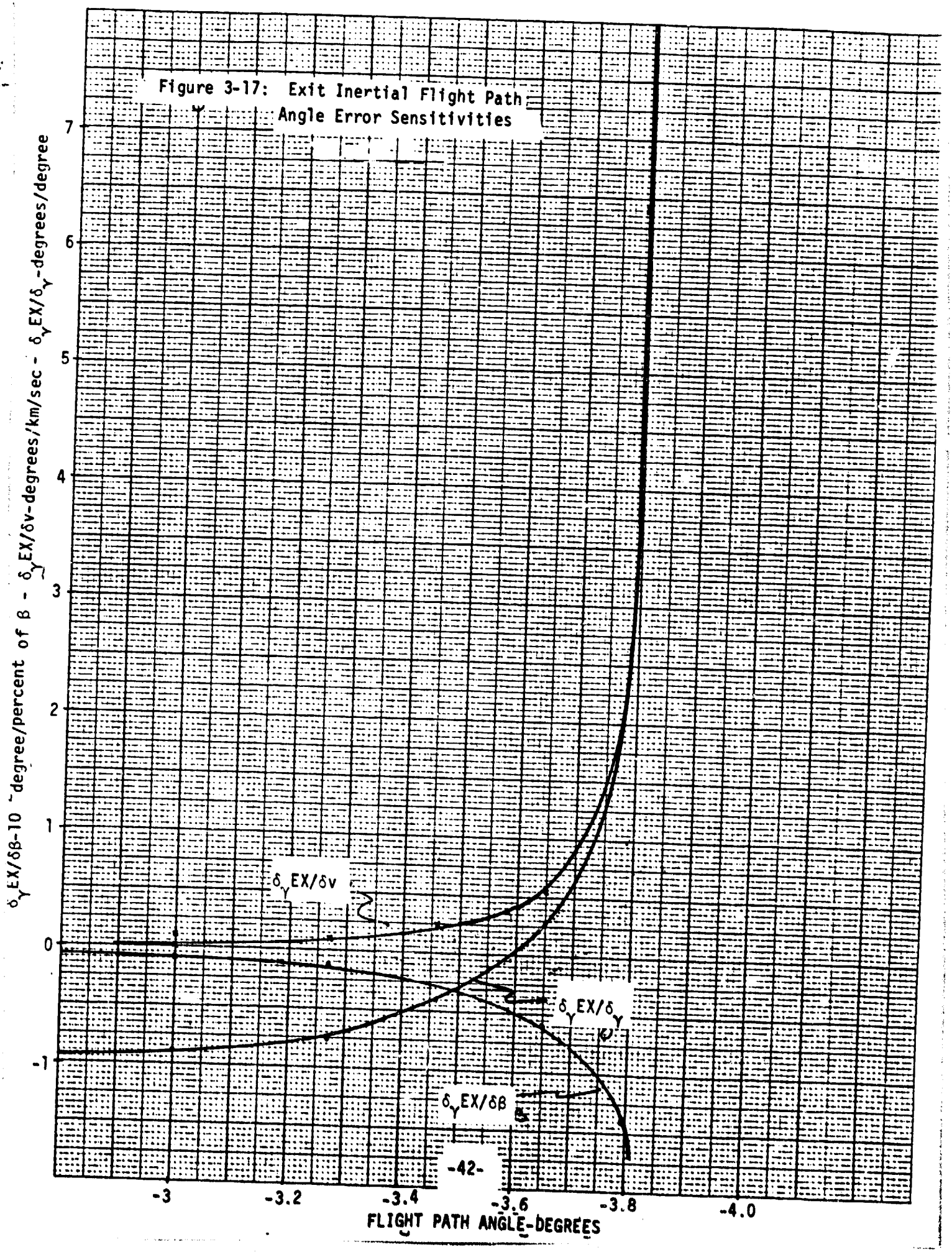

partials for the exit flight path angle. Sample values are given in Table 3-7.

The capture mode is thus seen to be categorized by high error sensitivities, and the attendant requirement for accurate control of encounter conditions (in the absence of onboard path control capability) to avoid uncontrolled direct entry of the vehicle. This consideration would tend to constrain the entry corridor towards the overshoot boundary. Note, furthermore, that the error sensitivities accumulate over subsequent passes (in the absence of correction maneuvers), causing large uncertainties as to the eventual terminal (landing) conditions.

3.4.2 Ballistic Coefficient Effects

Figure 3-18 presents exit velocity as a function of the encounter flight path angle for the reduced ballistic coefficient vehicle, for maximum relative velocity encounter. For comparison purposes, the corresponding curve for the baseline vehicle is also included.

Comparison of these two curves indicates that modification of the vehicle ballistic coefficient simply shifts the range of acceptable encounter conditions, but neither widens the corridor nor reduces the error sensitivities within it.

3.4.3 Lifting Vehicles

The addition of a lifting capability, however, does significantly modify the capture performance. This is illustrated in Figure 3-19, which presents exit velocity as a function of encounter flight path angle for various vehicle L/D ratios. Comparison of these curves to Figure 3-12 clearly exhibits the widening of the entry corridor and attendant reduction of error sensitivity with increasing L/D.

It should be noted that, for a lifting vehicle, it is possible for atmospheric exits to occur at less than circular velocity; the vehicle, however, will re-enter the atmosphere less than half a revolution from the exit point.

Finally, Figure 3-20 presents the exit inertial flight path angle for the same set of vehicle L/D ratios.

Table 3-7: Baseline Ballistic Vehicle Exit Velocity and Flight Path Angle Error Sensitivities

Flight Path Angle-degrees	$\partial v_E/\partial v$ m/sec/m/sec	$\partial v_E/\partial \gamma$ m/sec/degree	$\partial v_E/\partial B$ m/sec/percent of B	$\partial \gamma_E/\partial v$ degree/m/sec	$\partial \gamma_E/\partial \gamma$ degree/degree	$\partial \gamma_E/\partial B$ degree/percent of B
-3	1.12	463.7	- 2.86	0	- .88	-8.6×10^{-4}
-3.27	1.26	930.3	- 5.0	1.15×10^{-4}	- .76	-1.33×10^{-3}
-3.46	1.47	1585.1	- 7.9	2.4×10^{-4}	- .40	-3.4×10^{-3}
-3.65	1.95	2897.5	-13.7	5.61×10^{-4}	.27	-5.8×10^{-3}
-3.795	2.74	4930.15	-22.9	6.42×10^{-3}	6.86	-1.4×10^{-2}

INTERMETRICS INCORPORATED • 701 CONCORD AVEN. - MBRIDGE, MASSACHUSETTS 02138 • (617) 661-1840

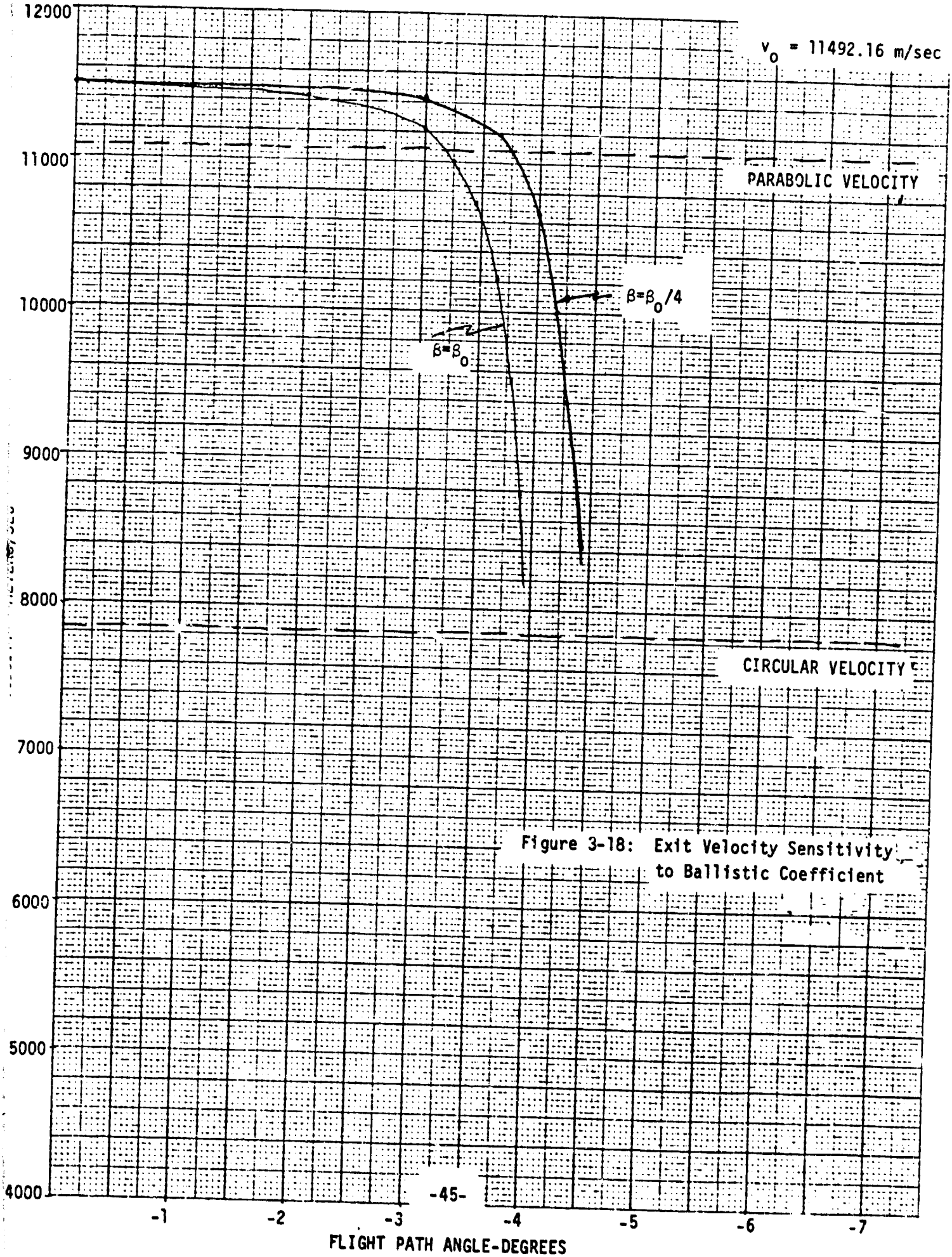

Figure 3-18: Exit Velocity Sensitivity to Ballistic Coefficient

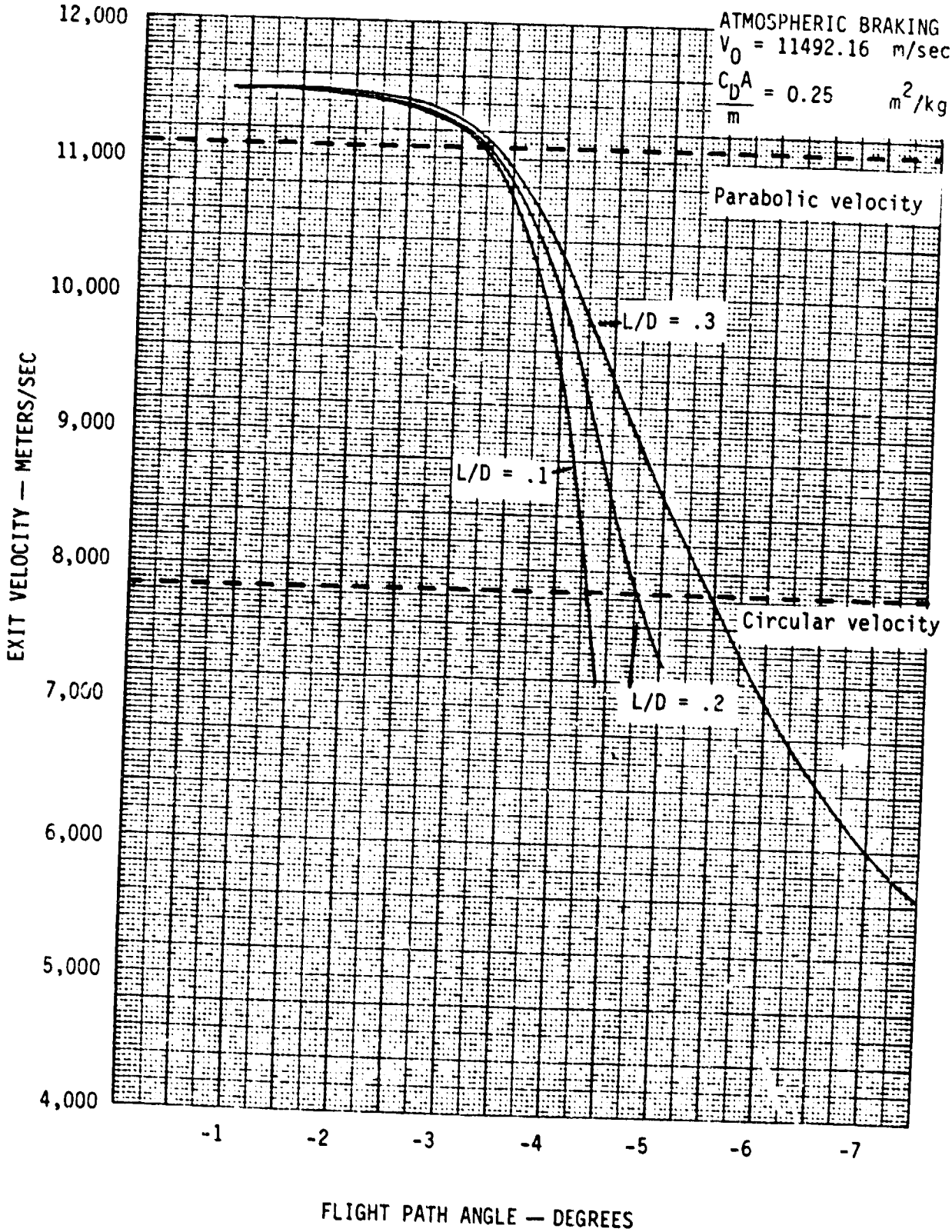

Figure 3-19: Exit Velocity Sensitivity To Lifting Capabilities

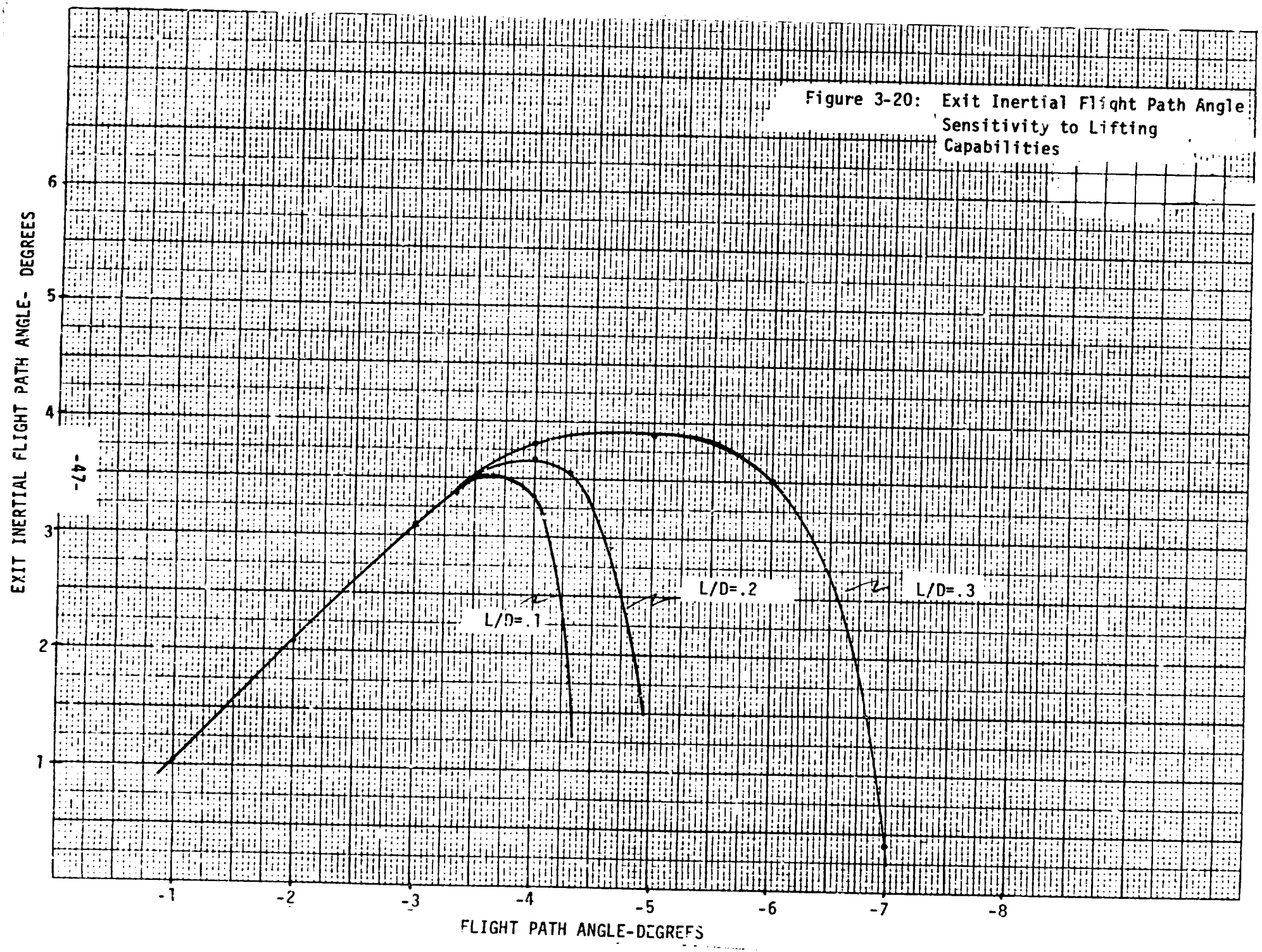

Figure 3-20: Exit Inertial Flight Path Angle Sensitivity to Lifting Capabilities

4.0 Maneuvering Vehicles

4.1 Introduction

In this section we consider vehicles with a propulsive maneuvering capability. Two cases of application of this capability are analyzed:

i) Establishment of initial capture orbit through thrust deceleration of the returning vehicle on an hyperbolic orbit.

ii) Perigee modifications of initial orbit established either through thrust deceleration or atmospheric braking.

The first maneuver can be used to park the returning vehicle in an orbit about the earth without incurring the high sensitivities encountered in Section 3.4 for atmospheric braking. Furthermore, the resulting orbit is stable since the resulting perigee is not forced to be within the atmosphere.

Following this initial capture, the vehicle's kinetic energy can be dissipated by lowering the perigee into the earth's atmosphere. Proper placing of the perigee altitude allows establishment of a controlled rate of orbital decay to a set of conditions from which either direct atmospheric entry in a more benign environment or orbital recovery by a space transportation system (i.e., Space Shuttle) can be effected.

This second maneuver can also be applied to rectify the orbit resulting from an atmospheric braking pass. In this case, however, orbital decay control may require either lifting or lowering of the orbit's perigee.

4.2 Thrust Braking

We consider thrust impulses applied at the hyperbolic perigee in

direction opposite to the velocity vector at that point. The impulsive velocity change required to place the vehicle on an elliptic orbit of eccentricity e is given by

$$\Delta v = \sqrt{2\mu/r_p + v_\infty^2} - \sqrt{\mu(1+e)/r_p} \qquad (4\text{-}1)$$

The apogee radius of the resulting orbit is then

$$r_a = r_p(1 + e)/(1 - e) \qquad (4\text{-}2)$$

Figure 4-1 presents the resulting apogee altitudes above the earth as a function of the applied velocity change for two values of perigee altitude: h_p = 150 kms and h_p = 1000 kms.

The corresponding orbital period is given by

$$P = 2\pi \sqrt{a^3/\mu}$$
$$a = (r_p + r_a)/2 \qquad (4\text{-}3)$$

and is plotted vs. the apogee altitude for the two values of perigee altitude in Figure 4-2.

It is therefore apparent that modest thrusting maneuvers ($\Delta v \sim 600 - 1000$ m/sec) are sufficient to capture the vehicle into earth orbit. Recovery with space transportation systems, such as the Shuttle, however, would require significant further reductions in perigee velocity, or, equivalently, significant reductions in orbit apogee altitude.

4.2 Perigee Modification Maneuvers

The additional required deceleration may be achieved, at modest cost, by lowering the orbital perigee into the atmosphere and exploiting the resulting drag force. Once the desired vehicle state is obtained, Shuttle

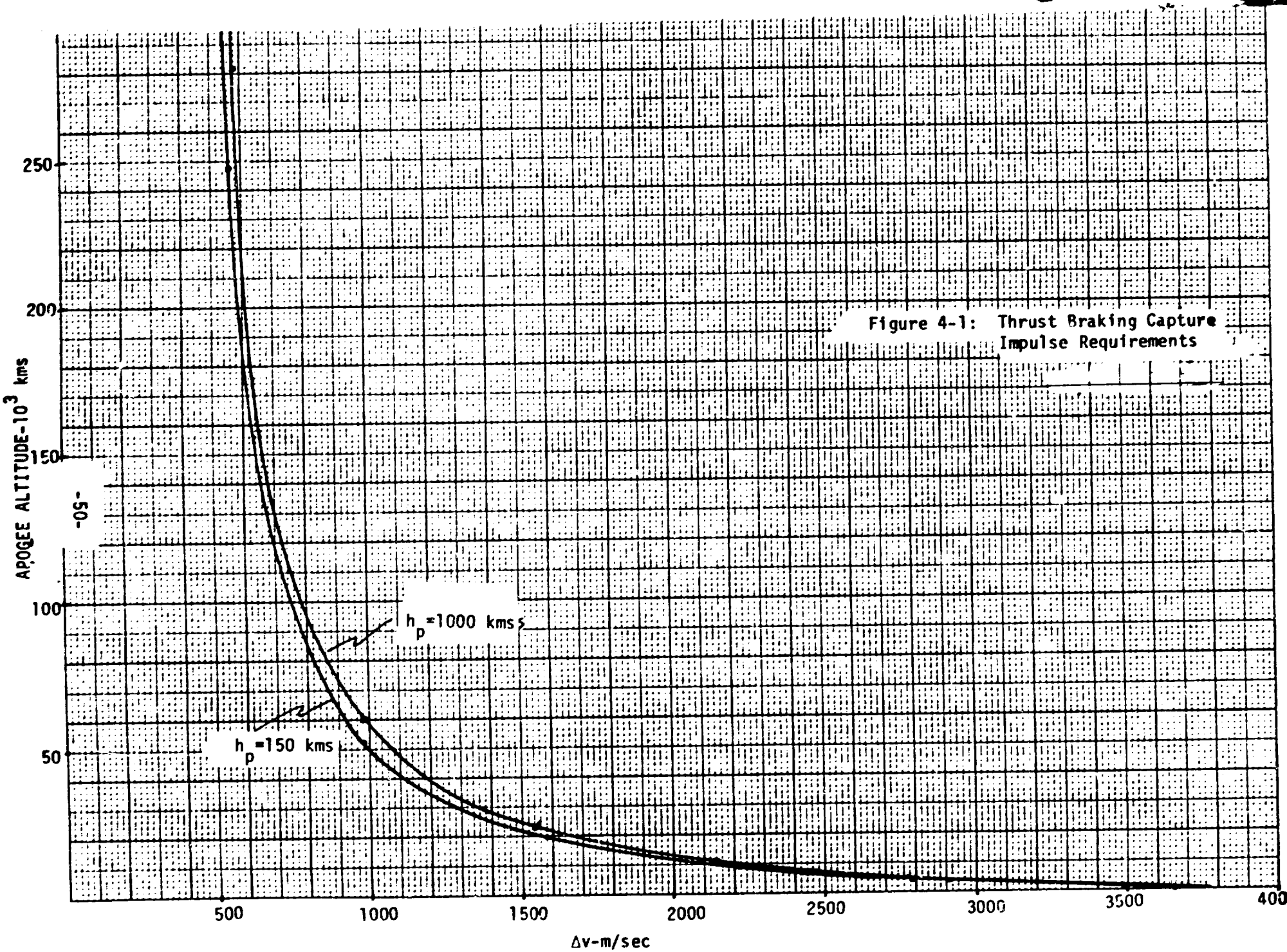

Figure 4-1: Thrust Braking Capture Impulse Requirements

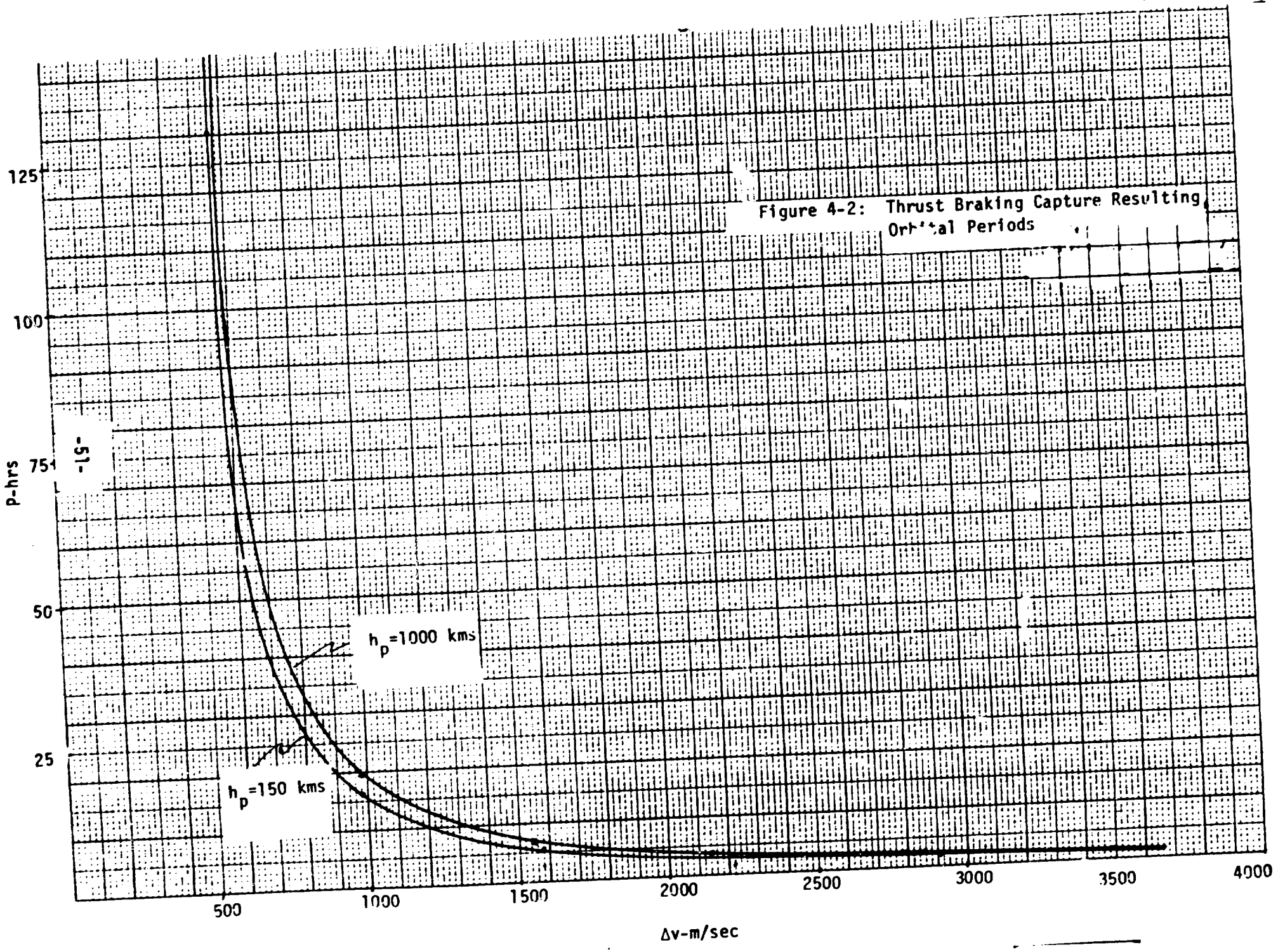

Figure 4-2: Thrust Braking Capture Resulting Orbital Periods

recovery may be effected, or the perigee may be raised to place the vehicle into a stable, but lower energy orbit. Alternatively, the vehicle may be allowed to decelerate to the point where encounter with the atmosphere will cause it to undergo direct entry and landing.

A similar scenario can be visualized for the atmospheric braking capture mode analyzed in Section 3.4. Following the initial pass through the atmosphere, a perigee rectification thrust maneuver could be applied to either raise the perigee out of the atmosphere to yield a stable orbit, or simply place the perigee at such an altitude that a controlled amount of deceleration will be effected during the next atmospheric pass.

In either case, application of the velocity change impulse at apogee is assumed. For small applied impulses, the resultant change in perigee altitude is given by

$$\Delta h_p = (2P/\pi) \sqrt{r_p/r_a}\, \Delta v \qquad (4\text{-}4)$$

The change in perigee altitude due to a unit velocity impulse Δv is plotted in Figure 4-3 versus the orbit apogee altitude for two values of perigee altitude.

4.3 Orbital Decay

Given that the orbit's perigee is within the atmosphere, the vehicle will experience a period of deceleration in each revolution. The resulting velocity change can be approximately considered as a tangential velocity impulse applied at perigee. Its major effect, therefore, will be a reduction in apogee altitude, given, analogously to Equation (4-4), by

$$\Delta h_a = (2P/\pi) \sqrt{r_a/r_p}\, \Delta v \qquad (4\text{-}5)$$

In actuality, a reduction in perigee altitude will also result, but this effect will be minor except in the immediate vicinity of the atmospheric braking corridor undershoot boundary. This fact was illustrated in Figure

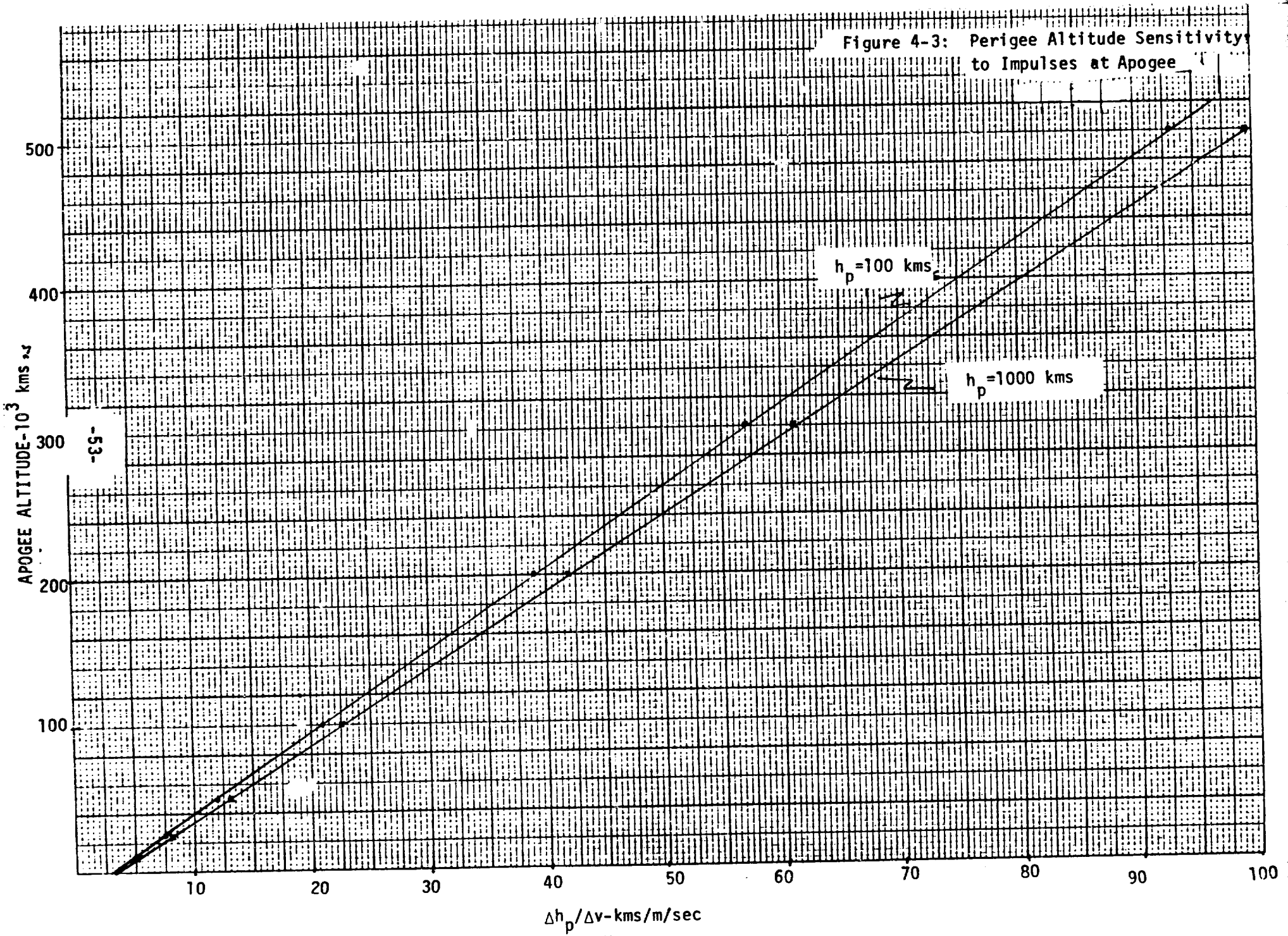
Figure 4-3: Perigee Altitude Sensitivity to Impulses at Apogee
h_p=100 kms
h_p=1000 kms
APOGEE ALTITUDE-10^3 kms
500
400
300
200
100
10
20
30
40
50
60
70
80
90
100
$\Delta h_p/\Delta v$-kms/m/sec

3-15 of Section 3.4.1, which presented the decay in perigee altitude for the atmospheric braking maneuver resulting orbits.

Figure 4-4 presents the apogee altitude decay over several revolutions for an initial apogee altitude of 31245.3 kms, and parameterized over various perigee altitudes. It can be seen from the figure that, given proper perigee placing, reasonably stable decay rates of apogee are achievable which allow maintenance of orbital flight over several revolutions.

Note, however, that the apogee altitude change is directly proportional to the applied deceleration. For highly eccentric orbits, Equation (4-5) can be approximately rewritten as

$$\Delta h_a \approx 2 r_p \Delta v / v_a \qquad (4\text{-}6)$$

where v_a is the velocity at apogee. On the other hand, as shown in Section 3.4, the applied deceleration is highly sensitive to the atmospheric encounter flight path angle.

The encounter flight path angle for highly eccentric orbits is defined by the perigee altitude. For a parabolic approach, the encounter flight path angle error is given by

$$\delta\gamma = -\delta r_p / 2\sqrt{r_p(r_{at} - r_p)} \qquad (4\text{-}7)$$

where r_{at} is the atmospheric edge radius.

The sensitivity of apogee altitude decay to errors in the location of perigee can then be approximately expressed, for highly eccentric orbits, as

$$\partial(\Delta h_a)/\partial r_p = \frac{2r_p}{v_a}\left(\frac{\partial(\Delta v)}{\partial\gamma}\right)\left(\frac{\partial\gamma}{\partial r_p}\right) = -\frac{1}{v_a}\sqrt{\frac{r_p}{r_{at} - r_p}}\left(\frac{\partial(\Delta v)}{\partial\gamma}\right) \qquad (4\text{-}8)$$

Neglecting the variations of $(\partial(\Delta v)\cdot/\partial\gamma)$ with small changes in encounter velocity allows using the curves of Figure 3-12 to represent this

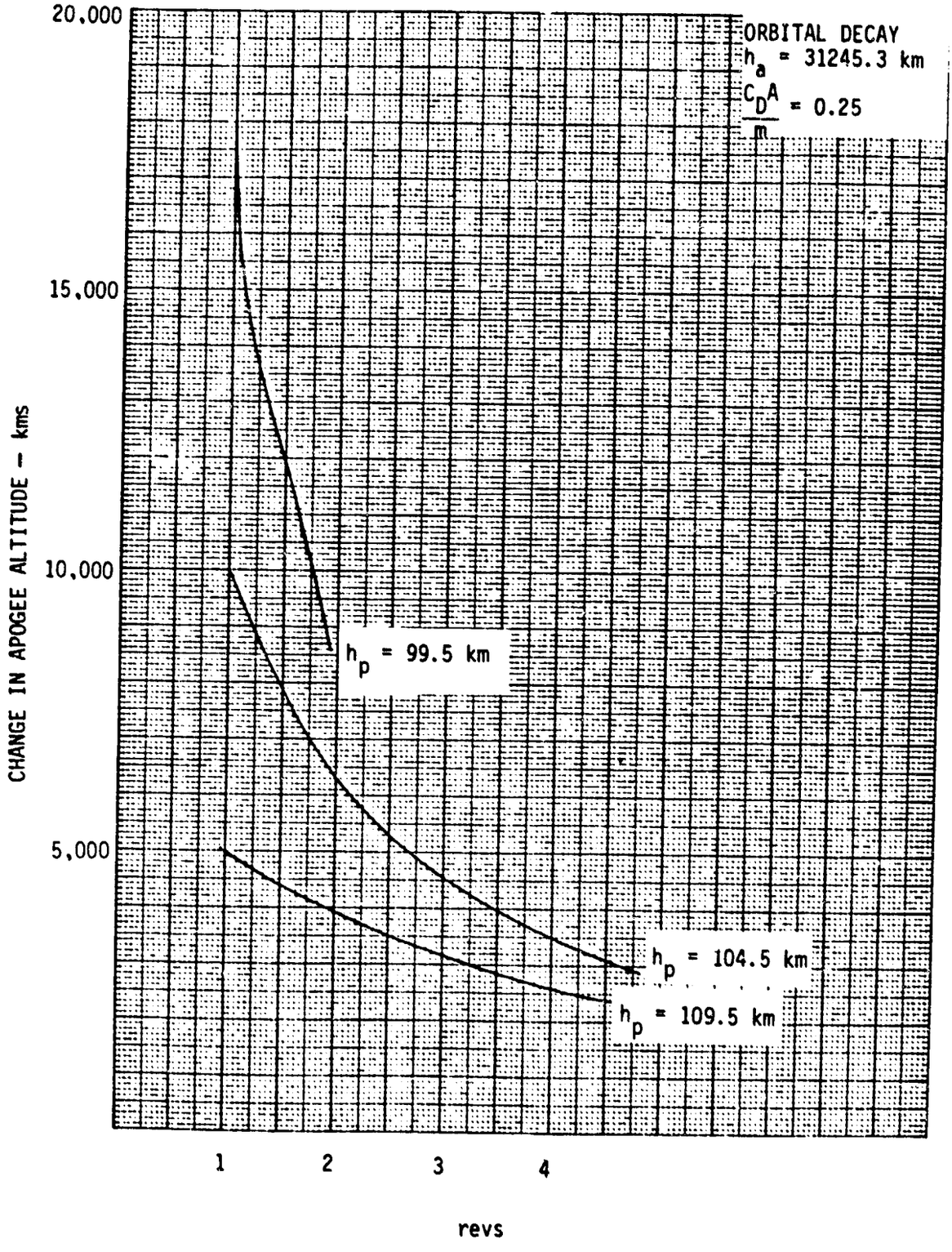

Figure 4-4: Apogee Decay for Multiple Atmospheric Passes

parameter. Utilizing the additional approximations

$$v_a^2 \approx 2\mu\, r_p / r_a^2 \tag{4-9}$$

Equation (4-8) is rewritten as

$$\frac{\partial(\Delta h_a)}{\partial r_p} = - \frac{r_a}{\sqrt{2\mu(r_{at} - r_p)}} \frac{\partial(\Delta v)}{\partial \gamma} \tag{4-10}$$

The sensitivity $\partial(\Delta h_a / r_a)/\partial r_p$ is plotted in Figure 4-5 versus the perigee altitude.

The generated sensitivity curve is only truly applicable for approximately parabolic orbits. A more complete analysis of these effects would require generation of velocity change sensitivity curves of the form of Figure 3-12 for the range of possible encounter velocities. This effort has not been undertaken in this study.

5.0 System Requirements

Chapters 3 and 4 analyzed three distinct MSR capture and recovery methods: direct entry, atmospheric braking, and thrust deceleration. Each of these methods presents requirements on system capabilities in order to meet constrained envelopes of desired terminal conditions.

Interactions of the vehicle with the earth's atmosphere were seen to be characterized by high error sensitivities, unless substantial vehicle stresses, in the form of structural loading and heating rates, could be endured. Thus, restrictions on allowable landing dispersions, or on acceptable atmospheric re-exit conditions, will generally require the provision of a guidance and control capability to maneuver the vehicle towards the desired terminal condition envelope.

On the other hand, vehicle maneuvers involved in the thrust deceleration capture mode, or for orbit rectification following the initial atmospheric braking pass, imply the provision of an impulsive capability to effect the velocity changes required, and of some means to control their direction and magnitude.

This chapter analyzes these system requirements. Sections 5.1, 5.2, and 5.3 discuss guidance and control requirements for atmospheric deceleration modes, while Section 5.4 discusses thrusting maneuver requirements.

5.1 Guidance Baseline

We are concerned with controlling terminal conditions in the form of down-range for the direct entry mode and of exit velocity and flight path angle for the atmospheric braking maneuver. It should be noted that the guidance and control capability could be utilized to condition other

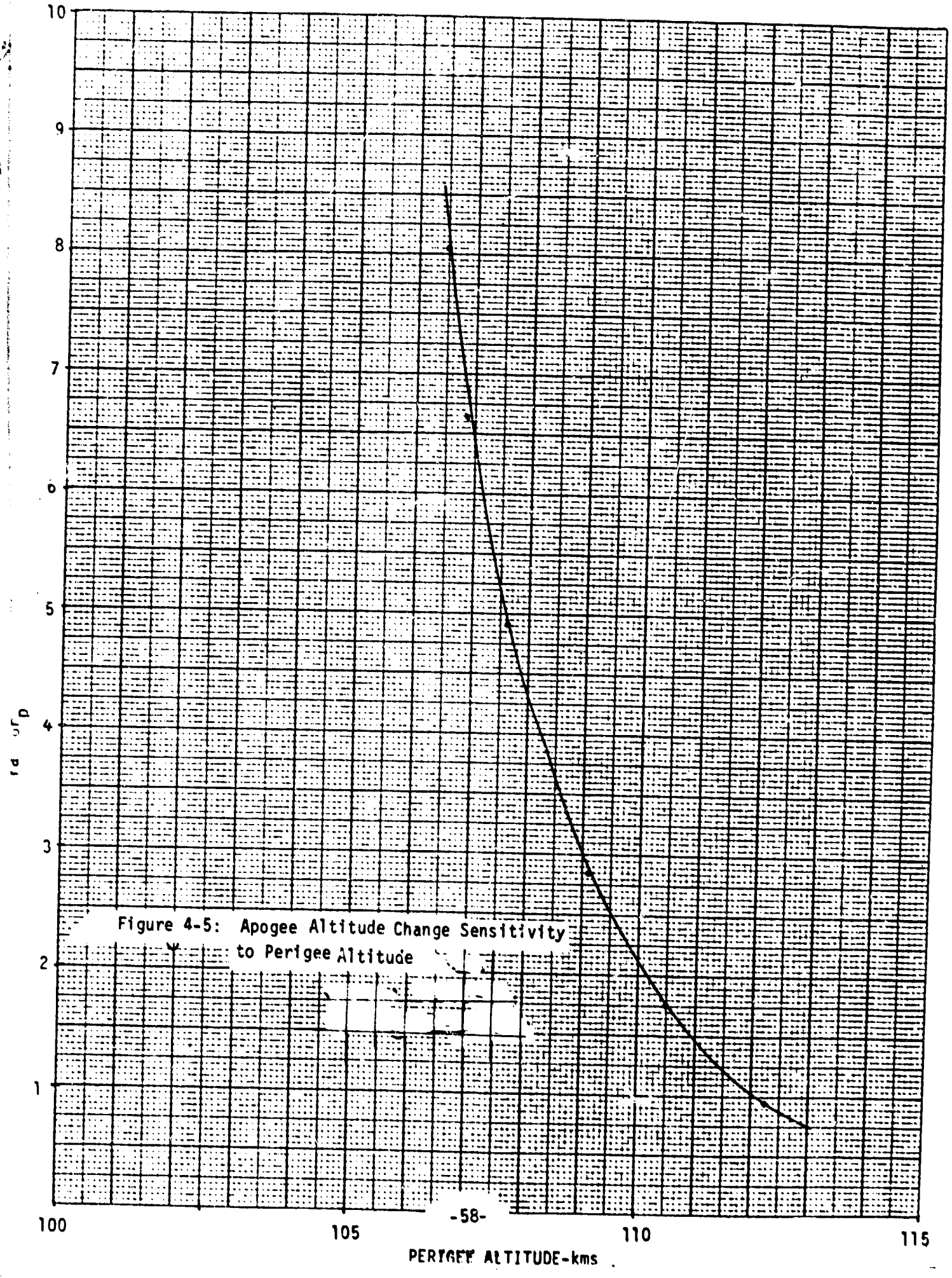

Figure 4-5: Apogee Altitude Change Sensitivity to Perigee Altitude

trajectory parameters (such as vehicle stresses); however, these considerations are not a subject of this discussion.

The available control force is assumed to be aerodynamic, i.e., lift. The control parameter is then the magnitude of the lift vector component in the up direction (e.g., fixed L/D vehicle with roll control of Apollo).

The two considerations of primary interest in specification of system requirements for support of atmospheric interface capture modes, are

- control envelope
- mean-square terminal error

The first consideration assumes perfect knowledge of the state of the vehicle and perfect derivation of control commands, and is concerned with specifying the control capability, in the form of a minimum vehicle L/D ratio, required to i) reach desired terminal conditions from constrained initial states, and ii) compensate for uncertainties in initial conditions and disturbances along the path.

Thus, the provision of a control capability may allow the specification of a common landing site for the whole family of expected MSR return trajectories, which might not be reachable through ballistic direct entries due to constraints on return orbit inclination and allowable vehicle stresses (see Section 3.3).

On the other hand, the atmospheric encounter process was seen to be characterized by high error sensitivities. Chapter 3 indicated that the primary error source in this process is uncertainty as to the atmospheric encounter flight path angle. The provision of a control capability thus conceptually permits compensation of a range of these errors by steering the vehicle to the desired terminal conditions from the offset initial state.

The second consideration establishes the accuracy of the guidance and control system required to determine deviations from the nominal path and to generate corrective actions. In the presence of uncertainty, it is not possible, in general, to meet desired terminal conditions with zero

error. Instead, we are forced to consider minimization of terminal errors in a statistical or mean-squared sense.

The certainty-equivalence principle or separation theorem of optimal control indicates that the covariance of terminal errors is equal to the sum of the estimation error covariance and the control error covariance. Given that the covariance matrices are positive semidefinite, it is clear that mean-square terminal errors can never be made smaller than the mean-square errors in estimating them, regardless of the control logic used. We will then assume that the optimal control shall be utilized, and will concentrate on the accuracy requirements of the estimator.

During the atmospheric trajectory, a plasma sheath will form around the vehicle, blacking out all external communications. The navigation sensors utilized for estimation of trajectory deviations must therefore be self-contained to the vehicle. A standard sensor for this application is an inertial navigation system (INS).

We are therefore concerned with terminal condition estimation errors of the INS resulting from initial errors at atmospheric encounter (i.e., alignment) and instrument (i.e., gyro, accelerometer) errors which disturb the propagation of the estimated state along the path.

5.2 Direct Entry

We determine the set of reachable states, for given encounter conditions, by considering the range of terminal conditions between those achieved by full-up and full-down control. Figure 3-1 presented resultant down-ranges for a ballistic vehicle as a function of encounter flight path angle, and Figures 3-3 and 3-4 translated these into achievable landing latitudes. Figure 3-10, on the other hand, presented these down-ranges for fixed L/D vehicles will full-up lift. A new set of landing latitudes could then be similarly obtained. Furthermore, a third family of curves could be generated under the assumption of full-down lift, with a corresponding set of landing latitudes. The range of landing latitudes, for a given encounter flight path angle and orbital inclination, represents the set of reachable impact latitudes for the selected vehicle L/D ratio.

From Figures 3-1 and 3-10 it is clear that a broad set of controllable errors exists for minimum lift capabilities. For example, assume a nominal trajectory with encounter flight path angle of -7.5° at maximum relative velocity entry. The resultant down-range is 548 kms. At full-up lift, this down-range is achieved with an encounter flight path angle of -9° for L/D = .1 and -11.5° for L/D = .2. Therefore, encounter flight path angles uncertainties of 1.5° for L/D = .1 and 4° for L/D = .2 are controllable with up lift.

Evaluation of INS terminal condition estimation error sensitivities requires selection of a nominal trajectory, since some of the involved error sources are dynamic. The selected nominal corresponds to maximum relative velocity entry of baseline ballistic vehicle at an encounter flight path angle of -7.5°. Characteristics of this entry path were given in Table 3-3.

The results presented here have been generated utilizing a space-stable INS mechanization model, so no sensitivities to gyro torquer scale factors, or gyro misalignments will be presented. Furthermore, to obviate the implications of relative alignment of instrument axes with the operating drag force, the results are presented for general types of error sources, rather than for individual components.

Table 5-1 presents down- and cross-range terminal errors resulting from unity INS error sources, including initial alignment errors, accelerometer biases, scale factors and misalignments, and gyro biases and g-sensitive drifts. The presented values thus reflect individual error source influence functions onto the INS estimated terminal state. In addition, given the short time of flight intervals relative to the Schuler period, it can be expected that initial position errors translate directly into corresponding terminal errors, and that initial velocity errors integrate in similar open loop fashion.

Table 5-1: INS Error Source Influence Functions - Direct Entry Maneuver

Error Source	Cross-Track Position [m]	Down-Track Position [m]
Initial Stable Member Misalignment (mrad)	9214	9870
Accelerometer Input Axis Misalignment (mrad)	9214	8620
Accelerometer Bias (100 μg)	743	744
Accelerometer Scale Factor (100 ppm)	-	926
Gyro Bias (degree/hour)	19000	19264
Gyro Acceleration Sensitive Drift (degree/hour/g)	29911	27900

INTERMETRICS INCORPORATED • 701 CONCORD AVENUE • CAMBRIDGE, MASSACHUSETTS 02138 • (617) 661-1840

It was indicated in Chapter 3 that these direct entry trajectories consist of a short high-deceleration segment and a longer equilibrium fall. For passive, aerodynamically controlled vehicles (e.g., fixed L/D), most of the control capability is concentrated in the initial high deceleration segment, with little control force available during the longer equilibrium regime. An alternate view of the control problem is then that of matching a desired set of equilibrium fall insertion conditions, in which case INS estimation errors accumulating after this point cannot significantly influence the eventual terminal conditions. The parameters of interest are then estimation errors at the end of the high deceleration segment.

These influence functions are presented in Table 5-2. Down- and cross-range errors at this point will directly translate into terminal errors.

5.3 Atmospheric Braking

The set of reachable states for this mode is determined by consideration of Figures 3-12, 3-19, and 3-13 and 3-20. Generation of a third family of curves reflecting the application of full-down control then allows determination of the range of exit velocities and flight path angles reachable from a given encounter flight path angle.

Similarly, the range of controllable errors is evident from these curves. For example, consider a maximum relative velocity encounter at a flight path angle of -3.7°. The resulting exit velocity is then 10 kms/sec. Alternately, this exit velocity is achievable with an encounter flight path angle of -3.85° for L/D = .1; -4° for L/D = .2, and -4.15° for L/D - .3. The range of controllable errors (for up lift) is then .15° for L/D = .1; .3° for L/D = .?; and .45° for L/D = .3.

The evaluation of INS estimation accuracy has been carried out for a nominal trajectory corresponding to maximum relative velocity encounter of the baseline ballistic vehicle at an encounter flight path angle of -3.65°. The INS model again represents a space stable mechanization.

Table 5-2: INS Error Source Influence Functions at t=200 secs - Direct Entry Maneuver

Error Source	Cross-Track Position [m]	Down-Track Position [m]
Initial Stable Member Misalignment (mrad)	1786.0	267.0
Accelerometer Input Axis Misalignment (mrad)	1783.0	393.0
Accelerometer Bias (100 μg)	19.3	19.3
Accelerometer Scale Factor (100 ppm)	-	178.0
Gyro Bias (degree/hour)	381.0	86.8
Gyro Acceleration Sensitive Drift (degree/hour/g)	2934.05	586.2

Table 5-3 presents influence functions of INS initial alignment error and instrument errors on exit velocity and flight path angle. Note that, due to the short duration of this path, gyro error effects are negligible, as they do not integrate into significant platform misalignments unless extraordinarily large error coefficients are assumed (>> 1°/hr). Therefore, they are excluded from the table.

In addition to the presented sensitivities, it can be expected that initial position and velocity errors will directly translate into terminal flight path angle and velocity estimation errors.

Table 5-3: INS Error Source Influence Functions - Atmospheric Braking Maneuver

Error Source	Exit Velocity Error [m/sec]	Exit Flight Path Angle Error [mrads]
Initial Stable Member Misalignments (mrad)	.17	.12
Accelerometer Input Axis Misalignments (mrad)	.12	.01
Accelerometer Bias (100 μg)	.15	.015
Accelerometer Scale Factor (100 ppm)	.12	.003

INTERMETRICS INCORPORATED • 701 CONCORD AVENUE • CAMBRIDGE MASSACHUSETTS 02138 • (617) 661-1840

6.0 Inertial Subsystem Mechanizations

In order to perform guided propulsion or aerodynamic maneuvers, it is necessary to determine and maintain an estimate of vehicle attitude, and possibly specific force, depending on the type of guidance. In this chapter some specific hardware alternatives will be described, along with their implementation characteristics as regards complexity and reliability.

6.1 Strapdown vs. Gimballed

6.1.1 Gimballed Inertial Subsystems

This type of implementation consists of a gimballed stable member, upon which are mounted gyro torque sensors and accelerometers. Once the inertial orientation has been determined, it is possible to maintain this estimate without the explicit intervention of attitude computations or other data processing functions; attitude excursions which result in torques applied to the stable member are sensed by the gyros, and counter torque commands are fed back to motors mounted on the gimbal axes. As the gyro input axes can be used to define an inertial coordinate system, output from co-aligned accelerometers can be used directly to integrate a state vector maintained in this frame.

6.1.2 Strapdown Inertial Subsystems

In this type of system, the input axes of the gyro and accelerometers have a fixed orientation with respect to the vehicle body axes. Given an initial estimate of body attitude with respect to some inertial frame, the changes in vehicle orientation are incrementally sensed and used to integrate the body-to-inertial transformation matrix. This matrix is then used to periodically convert accelerometer measurements to the reference navigation

coordinate system. Generally speaking the strapdown system offers less mechanical complexity at the cost of additional processing to utilize the outputs.

6.2 Gyro Types: Floated vs Dry

The floated gyro was the first of the two designs to reach maturity. A great deal of research and design effort went into the development of this concept during the 1940's, 50's and 60's. Many different gyro designs using this concept have been built and used over the years. Some further improvements in performance may still occur, but most R&D effort in the industry has now switched to the dry gyro.

Gimballed systems employing dry gyros became operational in the early 60's and satisfactory performance in strapdown applications has only been achieved in the last 5 years. The design is now relatively mature, although some performance improvements can still be expected in the next few years.

For critical applications, a properly designed floated gyro can still give better inertial performance than can a dry gyro. Where the dry gyro system can give satisfactory performance, however, it is generally preferred since the dry gyro is a less delicate and less expensive instrument, and usually results in a physically smaller and lighter system. In addition, since the dry gyro is a two axis instrument, while the floated gyro is a single axis instrument, the parts count will be reduced and/or the level of redundancy on the system increased, both of which have a favorable effect on the probability of successfully completing the mission.

6.3 Gimballed System Navigation Performance

This paragraph discusses what appear to be achievable performance levels for a gimballed dry gyro system; we then apply the sensitivities derived in Tables 5-1 and 5-3 to obtain estimates of the final errors for both direct entry and atmospheric breaking. It will be assumed that the system has a three axis gimbal set with one-speed resolver readouts on each axis. A four gimbal system would be more general, but it is felt that a three gimbal mechanization will not impose significant constraints on the current mission. The results

of these calculations are shown in Table A for direct entry and Table B for Atmospheric Braking.

6.3.1 Discussion of Error Sources

Examination of Tables A and B shows that in both cases, the error source which dominates the terminal errors is the initial stable member misalignment. This deserves some comment.

In order to align an inertial system, it is necessary to determine the orientation of the stable member with respect to the fixed stars, or equivalently, with the coordinate system of the earth plus a knowledge of time. For the assumed IMU in the MSR vehicle, this is accomplished by using a star sensor or similar device to establish the direction of two or more stars with respect to the vehicle. These directions are then transferred to the stable member coordinates system using the gimbal angle readouts, in this case, the one-speed resolvers.

TABLE A

Error Source	Error (1σ)	Cross Track Error (m)	Down Range Error (m)
Inital Stable Member Misalignment	1.16 mr (4 $\widehat{\text{min}}$)	10688	11449
Accelerometer Input Axis Misalignment (non-Orthogonality)	0.73 mr (15 $\widehat{\text{sec}}$)	673	629
Accelerometer Bias	50μG	372	372
Accelerometer Scale Factor	75 ppm	-	695
Gyro Bias	.015 deg/hr	285	289
Gyro Acceleration Sensitive Drift	.02 deg/hr/G	589	558
	RSS	10735	11510

INTERMETRICS INCORPORATED • 701 CONCORD AVENUE • CAMBRIDGE MASSACHUSETTS 02138 • (617) 661-1840

TABLE B

Error Source	Error (1σ)	Exit Velocity Error [m/sec]	Exit Flight Path Angle Error [mrads]
Initial Stable Member Misalignments	1.16 mr	.197	.139
Accelerometer Input Axis Misalignments	.073 mr	.00876	.00073
Accelerometer Bias	50μG	.075	.0075
Accelerometer Scale Factor	75 ppm	.09	.00225
	RSS	.229	.139

INTERMETRICS INCORPORATED • 701 CONCORD AVENUE • CAMBRIDGE MASSACHUSETTS 02138 • (617) 661 1840

A resolver is an electromechanical device and is subject to many random and non-random errors. In the case of one-speed resolvers suitable for use on a small platform, these error sources will total 2 to 3 minutes of arc, 1σ. In addition, the resolver outputs must be converted to digital form for use in the navigation computer, thereby creating additional error sources, including the quantization error of the resolver to digital converter. This resolver plus converter error is the principal cause of the initial misalignment in our assumed system.

It should be noted that earth based systems (aircraft, shipborn, etc) are not subject to this error source. These systems are normally aligned by gyrocompassing, which uses the gyros and accelerometers on the stable member to determine the plane which includes both the earth's gravitation vector at the location in question and the earth's angular rotation vector. The line in that plane which is perpendicular to the gravitation vector is taken to be the North-South direction. This alignment is accomplished without any need to transfer direction information through the gimbals.

The problem of in-space alignment of gimballed inertial platforms has been attacked many times. In both the Apollo and the Space Shuttle manned space systems, multi-speed resolvers were added to all of the gimbal axes. This adds considerable complexity to the gimbal structure and to the resolver-to-digital converter. Other possibilities also exist, such as: 1) substituting a different, more accurate gimbal angle readout, 2) transfer the alignment information directly to the platform optically, bypassing the gimbals, or 3) somehow mount the star sensors inside the gimbals on the stable member. None of these solutions appear viable, and all would certainly be expensive.

6.4 Strapdown System Navigation Performance

With a strapdown system, the gimbals and resolvers are eliminated. along with the error contribution from the resolvers. There are other error sources, however, which contribute to the actual misalignment, including some which are not present in gimballed systems. One of these new error sources is the gyro torquer scale factor error.

In a strapdown system, the gyro must follow the motions of the vehicle. This is accomplished by closed loop torquing the gyro to null the error output, and sending the gyro torquing information to the digital computer, which integrates the incremental torquing information to keep track of the attitutde of the vehicle. The difference between the angular rate actually produced by the gyro torquing system and the angular rate used by the computer to keep track of vehicle attitude is the torquer scale factor error. This error contributes to the error in knowledge of the true vehicle attitude as an open loop integration, proportional to the total angle through which the vehicle rotates. Furthermore, the error terms for torquing of a gyro in opposite directions are in general not identical and in some implementations are substantially uncorrelated, so that oscillatory rotational motion of the vehicle leads to a growing error, not a cancellation of the error.

A reasonable value for the gyro torquer scale factor error in the type of system we are discussing is 75 ppm, 1σ. Exactly how this will couple into the errors in initial alignment and navigation performance during entry is difficult to predict until a specific operating scenario is available, but it is worth noting that this error will cause a .47 mr (1.61 $\widehat{\text{min}}$) error after a 2π radian rotation of the vehicle.

Other error sources which contribute to initial misalignment of the strapdown navigation system are mounting and machining errors between the navigation system base and the star sensors, errors in the star sensor itself, and gyro drift between the time of alignment and arrival at the beginning of the entry maneuver.

In connection with the last mentioned error, it should be noted that 0.015 deg/hr gyro bias rate assumed for the gimballed system , the alignment of the system deteriorates from this cause alone at 0.26 mr/hr (0.9 $\widehat{\text{min}}$/hr). On the other hand, with a strapdown system, it should be possible in a reasonable length of time to calibrate the gyro bias during the alignment process to a value of .003 deg/hr or better.

For a properly designed alignment procedure, a value of .29 mr (1.0 min) 1σ for the initial alignment of the system at entry interface appears reasonable. Using this value, the navigation performance of the system for the direct entry and atmospheric braking cases are shown in Tables C and D.

From these tables, we see that the initial misalignment is still the dominant error source for both down range and cross track errors for direct entry and for the flight path angle error with atmospheric braking, and that the RSS error estimates have been reduced almost in proportion to the reduction in alignment error. For the exit velocity error in the atmospheric braking case, the misalignment is no longer the dominant error source listed.

6.5 Operating Life and MTBF Estimates

For both the gimballed and the strapdown versions of the INS, operating lifetimes of 30,000 to 50,000 hours should be attainable. This should be adequate for the intended mission unless it is anticipated that the system will be left powered up continuously. Mechanical wear in the gyro bearings is usually the limiting factor in operating life.

For a basic, non-redundant, three axis inertial system, the MTBF will typically be in the range of 3000 to 5000 hours, for both gimballed and strapdown systems. The gimballed system has more electromechanical components such as torque motors, sliprings and resolvers, than the strapdown system, but the gyros of the strapdown system are subjected to a more severe environment, and the gyro torquer electronics are more complicated and operate at higher power levels. The differences essentially balance out.

If the MTBF value quoted above does not produce a high enough probability of mission success, one way to increase this probability of success is to add redundant components to the system such that the mission can still be completed with one or more failed components. This is another area in which the strapdown design has advantages over the gimballed design.

TABLE C

Error Source	Error (1σ)	Cross Track Error (m)	Down Range Error (m)
Initial Stable Member Misalignment	.29 mr (1 min)	2672.	2852
Accelerometer Input Axis Misalignment	0.73 mr (15 sec)	673	629
Accelerometer Bias	50μG	372	372
Accelerometer Scale Factor	75 ppm	-	695
Gyro Bias	.003 deg/hr	57	58
Gryo Acceleration Sensitive Drift	.02 deg/hr/g	589	558
	RSS	2843	3086

INTERMETRICS INCORPORATED • 701 CONCORD AVENUE • CAMBRIDGE MASSACHUSETTS 02138 • (617) 661-1840

TABLE D

Error Source	Error (1σ)	Exit Velocity Error [m/sec]	Exit Flight Path Angle Error [mrads]
Initial Stable Member Misalignment	.29 mr	.0493	.0348
Accelerometer Input Axis Misalignment	0.73 mr	.00876	.00073
Accelerometer Bias	50μG	.075	.0075
Accelerometer Scale Factor	75 ppm	.09	.00225
	RSS	.127	.0347

INTERMETRICS INCORPORATED • 701 CONCORD AVENUE • CAMBRIDGE, MASSACHUSETTS 02138 • (617) 661-1840

With gimballed systems, the only practical way to obtain significant redundancy is to completely duplicate the platform, inertial components and gimbal systems, however many times are required to obtain the desired level of redundancy. This is expensive in terms of both weight and power consumption especially since each additional system only adds one more level of failure tolerance. In other words, if the z gyro fails on one platform and the x accelerometer fails on another, both platforms are essentially out of operation.

With a strapdown system, effective redundancy can be added in much smaller increments. The stable member (navigation base) of a strapdown system is essentially a passive block of machined metal which has an extremely low probability of failure. A single, non-redundant, such navigation base can be used on the vehicle without significantly effecting the probability of mission success and furthermore, this base can easily be made large enough to accomodate redundant inertial components. By doing this, the loss of one of two redundant z gyro axes and one of two redundant x accelerometer axes will not put the system out of operation.

Another design feature which can effectively increase the redundancy level of a system without significantly increasing the weight or power is to mount the inertial components with their input axes at skewed angles rather than parallel and perpendicular to each other. By doing this, one component can effectively (with some degredation in performance) act as a redundant component for more than one other component. This is an area which has received considerable study, both theoretical and practical, but not all of this work is applicable to the current circumstance since much of it involved use of single input axis instruments rather than two input axis instruments. Several systems using these principals have been built and flown in space applications with good success.

This is an area which should receive additional study directed towards the particular current application. This is particularly true because with redundant hardware the simple value of a Mean Time To Failure is not a proper indication of the probability of successful completion of the mission. Instead, this probability is a more complicated function of the actual duration of the

mission, and the failure rates and levels of redundancy of each component.

6.6 Weight and Power Estimates

In this paragraph, estimates of the weight and power consumption of a gimballed and a strapdown inertial system are presented. The gimballed system is a non-redundant, three axis dry gyro system, and the strapdown system has a moderate level of redunancy, with three, two-axis dry gyros, either skewed or orthogonal-colinear and 4 or 6 single axis accelerometers, again either skewed or orthogonal-colinear. In each case, all supporting electronics including power supplies and power conditioning for operation from 28V DC source is included.

It turns out that the estimates for these systems, to within the accuracy that is possible at this time, are the same. Both systems, built with "conventional" space technology (aluminum structure, cold plate cooling, etc) and including a digital computer for the navigation calculations, will weigh between 20 and 25 kg and require 75 to 100 watts while operating. If another computer is available on the vehicle so that the navigation computer can be eliminated from the inertial system, a savings of 3 to 5 kg and 20 to 25 watts will be possible although there may be an offsetting increase in computer resource requirements.

By changing to a more "exotic" design(Beryllium structure, special hybrid electronics, special low power consumption circuits, etc) it may be possible to get the navigation system without a computer down to 12 to 15 kg and the power consumption down to 35 to 50 watts when operating. There is, however, considerable additional design cost and some technical risk involved in this approach.

With reasonable care in the design of the thermal environment in the vehicle, it should be possible to avoid the need to use heaters on the gyros when the system is not in use. Dry gyros are much less susceptible to damage from temperature extremes when not in operation than are floated gyros, so a less stringent thermal environment specification is possible.

6.7 Alternatives

If the navigation performance of the dry gyro configurations described in this chapter is found to be inadequate for the intended mission, the next step up in inertial component performance would be to switch to the older floated gyro technology. The costs associated with this change are 50% to 100% increases in estimated weight, some increase in operating power, and possibly a requirement for active temperature control of the gyros when the system is not in operation. It should be noted, however, that unless some way to increase the accuracy of the initial alignment can be found, there is little to be gained by increasing the performance of the inertial components.

6.8 Other Technologies

Several new gyro technologies are presently being studied and developed by a number of investigators, laser gyros and atomic gyros are included in this group. While these new technologies appear to have some promise, none of them are currently sufficiently mature to be baselined for the present application, and it appears that they will not be mature for a least another 3 to 5 years.

6.9 Limitations on Mission Profile

There are several practical limitations imposed on the mission profile by the requirements of the inertial instrumentation described in this chapter. Among these limitations are:

1) In order to obtain the assumed accelerometer performance, the peak acceleration during the mission should not exceed 10 to 15 G.

2) If the strapdown system is to be used, the limitations in gyro torquer capability will restrict the maximum angular rates of the vehicle to 200 to 400 degrees per second, and average rates over one second or more to 100 degress per second.

3) If the strapdown system is to be used, spin stabilization of the vehicle should be avoided if possible, If spin stabilization must be used, the strapdown design may not be applicable.

4) If the gimballed system is to be used and high angular rates are required, it would be preferred to have the outer gimbal axis parallel to the axis of rotation.

5) Final star sightings for alignment of the system should be provided as close to entry interface as practically possible.

6.10 Recommendation for Additional Study

There are two areas which it appears would benefit from further study at this time

1) Study of methods of obtaining better initial alignment of the navigation system.

2) Investigation of redundant hardware configurations based on the specific proposed mission profile to identify configurations having a high probability of mission success.

7.0 Risk Analysis

A quantitative analysis of the reliability of various recovery methods is possible in principle if a complete description of the critical systems is available, together with the failure modes of each component, the probability thereof, and a statistical description of the characteristic output of each component, given that it has failed. In fact, such information is generally not available with respect to similar equipment used for commercial purposes (such as inertial measurement units), and in any case, the rate of failure is so small that insufficient quantitative data are available to characterize the failed outputs. This chapter will therefore not attempt a detailed quantitative estimate of the reliability of various methods, but instead identify the key system components necessary for successful performance, and the effect of various failures on each of these. Such effects depend not only on the nature of the failure, but the flight regime of the vehicle at the point where the failure occurs. Possible outcomes of a given earth encounter sequence are taken to be:

a) Recovery of the sample module according to the constraints and protocol laid down for preservation of physical and biological integrity of the container.

b) Sample recovery involving violation of such constraints and protocol.

c) Loss of the sample module in the biosphere.

d) Loss of the sample module outside the biosphere.

7.1 Minimum Recovery System

As used in this paragraph, "minimum" implies that method of sample recovery which provides maximum reliability within the constraint of minimum weight. Based on the quantitative results of Chapter 5, it is concluded that such a system is constituted by an unguided direct entry vehicle, designed to enter at near vertical flight path angles. Such a system can be designed to be self orienting as aerodynamic forces become appreciable, and does not depend on the correct operation of on-board guidance and control equipment to attain nominal impact conditions. The absence of such equipment eliminates the corresponding weight, power, and thermal protection requirements, as well as associated failure modes. Since mechanical structure ages negligibly compared to mechanical and electronic components, pre-flight stress testing can "prove" the integrity of the entry module relative to the entry environment.

As will be discussed in the next paragraph, there remains an unavoidable failure mode connected with improper deployment from the trans-earth bus, or failure of the bus command and control capability resulting in uncontrolled entry. This mode is common to all recovery methods which target the sample module to enter or pass through the terrestrial atmosphere. In this respect it is believed that the unguided entry vehicle is preferable to all others as it limits the period of exposure to system failures to activities prior to deployment, rather than all the way through the aerodynamic phase.

7.2 Suggested Optimum Baseline

The analytical results presented in Chapter 5 cannot eliminate any of the recovery modes based on technical infeasibility. From verbal discussions with JSC and JPL personnel concerned with issues of physical and biological integrity, it seems clear that the preferred method of recovery will be that which is technically feasible and offers maximum protection against back-contamination of the terrestrial environment. For reasons discussed previously, it is concluded that the recovery method should not involve targeting the bus or sample module to enter or pass through the atmosphere. It is believed that further study will show that an earth orbital capture technique, using retropropulsion, can be designed such that there is no measurable probability of encounter with the biosphere for any failure mode, including uncontrolled burn of the

retro rocket to depletion. Failure to perform the maneuver nominally will result in no capture, or capture into an off-nominal stable, high energy orbit. System requirements to support this method are minimal in extent and performance:

1) Attitude determination can be by star tracker technology currently in use for similar missions,

2) Attitude control can be effected by cold gas thrusters or spin stabilization, both demonstrated techniques;

3) Retro - propulsion can be accomplished by a simple solid rocket motor, which burns to depletion after ignition;

4) Post-burn insertion orbit can be controlled by controlling approach conditions and ignition time.

Operational advantages include the permissibility of performing the orbital insertion maneuver even when the system status is suspect or biological integrity is known to be compromised; alleviation of severe orbit determination and trajectory control requirements; and the possibility of delayed recovery or on-orbit investigation of the sample module and its contents. Transfer of the sample to a terrestrial laboratory can be accomplished by remote recovery to Shuttle operational attitudes, whereupon the sample module can be placed in a Shuttle-born isolation cannister, guaranteed to withstand any catastrophic outcome of a Shuttle entry. Problems associated with this sequence will be discussed in the next chapter.

8.0 Orbital Recovery Operations

This chapter discusses the operational requirements to effect recovery of a sample module to a Shuttle payload environemnt. The most reliable flight vehicles available today are commercial passenger aircraft. These incorporate redundant mechanical and avionics components, and are designed to withstand stresses well above those to be encountered in normal conditions. As an aerodynamic vehicle, the Space Shuttle is subject to the same flight hazards as any manned aircraft, and to the additional hazard that it is a statically unstable vehicle through most of its flight regime, and unlike current airliners cannot be controlled without continuous computer assistance. As it is an unpowered vehicle, its navigational aids are flight critical except in the immediate vicinity of its landing field, under VFR conditions. The point of these observations is not to disparage Shuttle reliability, but to argue that this vehicle is not obviously more reliable than a commercial cargo aircraft. It therefore seems likely that special provisions for housing and protecting the sample module as a "hazardous cargo" will be required, just as they are with such materials in the case of domestic carriers.

8.1 Direct Recovery

In the case where the earth orbit injection module has further maneuvering capability, it may be possible to lower the apogee to within range of the Space Shuttle. This is currently expected to be in the vicinity of $(R_A + R_p)/2 \simeq 225$ n.m. without additional OAMS fuel in the payload bay, or about 300 n.m. with. In order to reach these altitutdes, the ground track of the bus must pass almost due east through KSC. The Shuttle currently provides rendezvous radar tracking on non-cooperating vehicles out to about 30 n.m., and to about 400 n.m. with a transponder. Although the transponder design is

available, there is currently no plan to develop one, and its provision is therefore a responsibility of the user. Use of the skin-tracking mode only is undoubtedly feasible with the Shuttle on-orbit navigation capability expected to be available at that time, provided that the target can be accurately located by ground tracking. The remaining question involves actual acquisition of the sample bus and placement in the payload cannister. This cannot be done with existing technology unless the bus is attitude stabilized and not spinning. The problems of achieving such stability or devising mechanisms for recovery of a non-cooperating bus, need further study.

8.2 Remote Recovery

At the present time, the best forseeable candidate for a remote recovery system is the space tug, not yet under development. If this is not available, a modified Interim Upper Stage is the alternative.

The Space Shuttle provides capability to perform rendezvous guidance and navigation, braking and station-keeping, as well as the payload manipulator system. All of these functions need to be incorporated in any remote recovery system, and the current plans for the tug or the IUS do not support this level of capability. It is the opinion of the authors that systems for performing remote retrieval will become available within the next ten years as an expansion of the overall capability of the space transportation system. If the remote retrieval option is decided upon, an immediate analysis of the performance requirements for the MSR mission should be undertaken, the results of which should be used to lend impetus and direction to the development of remote earth orbital operational capability. Bearing in mind that the cost of development can be spread over a number of customers, and the fact that remote retrieval is required in the case where a system failure eliminate the direct recovery option, this would seem to be the method of choice.

9.0 Open Issues and Future Studies

The most open issue associated with MSR earth recovery strategies is, and will continue to be, the level of reliability against back contamination which is necessary to gain acceptance of the mission objective. This report has argued that on the basis of system simplicity, performance requirements and weight, a direct entry, high flight path angle vehicle is the method of choice for a minimum system. This report has not addressed the question of structural, and hence weight, requirements for a vehicle which must pass through a 300 peak g profile, and impact at a speed of greater than 20 fps. Furthermore, the question of whether the earth encounter and deployment phase can be designed so as to offer an acceptable probability of uncontrolled entry remains unresolved. It is therefore recommended that the following two areas must be further evaluated for the minimum MSR:

a) Estimate of the weight of structure and thermal protection system for a high angle entry vehicle; and

b) Preliminary design of the earth encounter trajectory and deployment mechanism to minimize exposure to pre-deployment systems failures.

With respect to the recommended optimum baseline, the two most pressing issues are the conjecture that a guaranteed safe encounter/retrofire sequence can be constructed, and that suitable mechanisms will exist to recover a sample module above Shuttle operational altitudes. These areas can be further elucidated by

(i) A preliminary trajectory analysis of the approach path and retro sequence, to show no on-board failure can result in encounter with the earth atmosphere; and

(ii) A survey of potential needs for, and users of, remote operations and equipment for earth orbital applications. This survey should be oriented toward identifying common functional and performance requirements, and should result in a government/industry development effort.

APPENDIX A
MATHEMATICAL PROBLEM STATEMENT

A.1 Equations of Motion

Assuming that the vehicle possesses a stable configuration at zero roll, then all operating forces (i.e., drag, lift, gravity, centrifugal) are contained in the plane defined by the vehicle's velocity and position-relative-to-earth-center vectors. The motion of the vehicle relative to a spherical earth is described by [1]

$$\frac{dv}{dt} = -\frac{1}{2}\rho v^2 C_D A/m - g \sin\gamma$$

$$\frac{d\gamma}{dt} = \frac{1}{v}\left(\frac{v^2}{r} - g\right)\cos\gamma + \frac{1}{2}\rho v C_L A/m \qquad \text{(A-1)}$$

$$\frac{dh}{dt} = v \sin\gamma$$

$$\frac{dR}{dt} = \frac{r_e}{r} v \cos\gamma$$

$$\rho = \rho(h)$$

where

v	= earth relative velocity
ρ	= atmospheric density
γ	= flight path angle between velocity and local horizontal
h	= altitude above the earth
r_e	= earth radius
r	= vehicle radius = $r_e + h$
C_D	= vehicle drag coefficient
A	= vehicle reference area
m	= vehicle mass
$C_D A/m$	= B = ballistic coefficient
C_L	= vehicle lift coefficient
$\frac{1}{2}\rho v^2 B$	= D = drag acceleration
$\frac{1}{2}\rho v^2 C_L A/m$	= L = lift acceleration

L/D = lift to drag ratio

R = range = distance travelled over earth surface

Given the vehicle capabilities, as expressed in the ballistic coefficient B and the lift-to-drag ratio L/D, for example, the characteristics of the atmospheric environment, as expressed in a functional relationship of atmospheric density ρ to altitude h, and appropriate initial conditions for v, γ, h, these equations can be integrated in time to define the vehicle state at any desired instant.

The structural loading on the vehicle can be readily computed as the sum of the operating lift and drag forces. Its magnitude is simply

$$F = mD\sqrt{1 + (L/D)^2} \qquad \text{(A-2)}$$

The stagnation point convective and radiative heat rates are given by

$$\frac{dQ_C}{dt} = k_1(R_N)^{-1/2}(\rho/\rho_o)^{1/2}(v/1000)^{3.15}$$

$$\frac{dQ_R}{dt} = k_2(R_N)(\rho/\rho_o)^{3/2}(v/10000)^{12.5} \qquad \text{(A-3)}$$

where

Q_C = convective heat flow

Q_R = radiative heat flow

R_N = nose radius

v = velocity

ρ = atmospheric density

ρ_o = reference (surface) density

Except for extremely high velocities, the convective heat transfer is the dominant effect.

The total heat flow over the path is then obtained by integrating the heat rates in time and summing their contributions.

A.2 Initial Conditions

Integration of Equations (A-1) requires specification of initial conditions for the vehicle's earth relative velocity v, flight path angle γ, and altitude h.

The altitude at which aerodynamic flight is initiated is defined to be that of the outer edge of the earth's sensible atmosphere. This boundary is selected to be at an altitude above the earth's surface of 121.92 kms (400,000 ft), at which point the atmospheric density is of the order of 1.87×10^{-8} kgs/m^3.

For the Mars return hyperbolic orbits, the vehicle velocity,(relative to a non-rotating earth),is given, in terms of the orbit hyperbolic excess velocity v_∞, by

$$v_i = [2\mu/r + v_\infty^2]^{1/2} \qquad \text{(A-4)}$$

where

$\mu = 3.986012 \times 10^{14}$ m^3/sec^2 = earth gravitational constant

The corresponding flight path angle γ_i is most easily expressed in terms of the aim radius, r_a of the orbit relative to the target planet

$$\tan \gamma_i = \sqrt{(v_i^2 \, r^2/v_\infty^2 \, r_a^2) - 1} \qquad \text{(A-5)}$$

The geometry is illustrated in Figure A-1. The aim radius, which is equal to the semi-minor axis of the approach hyperbola, is given in terms of the desired vacuum perigee altitude, r_p

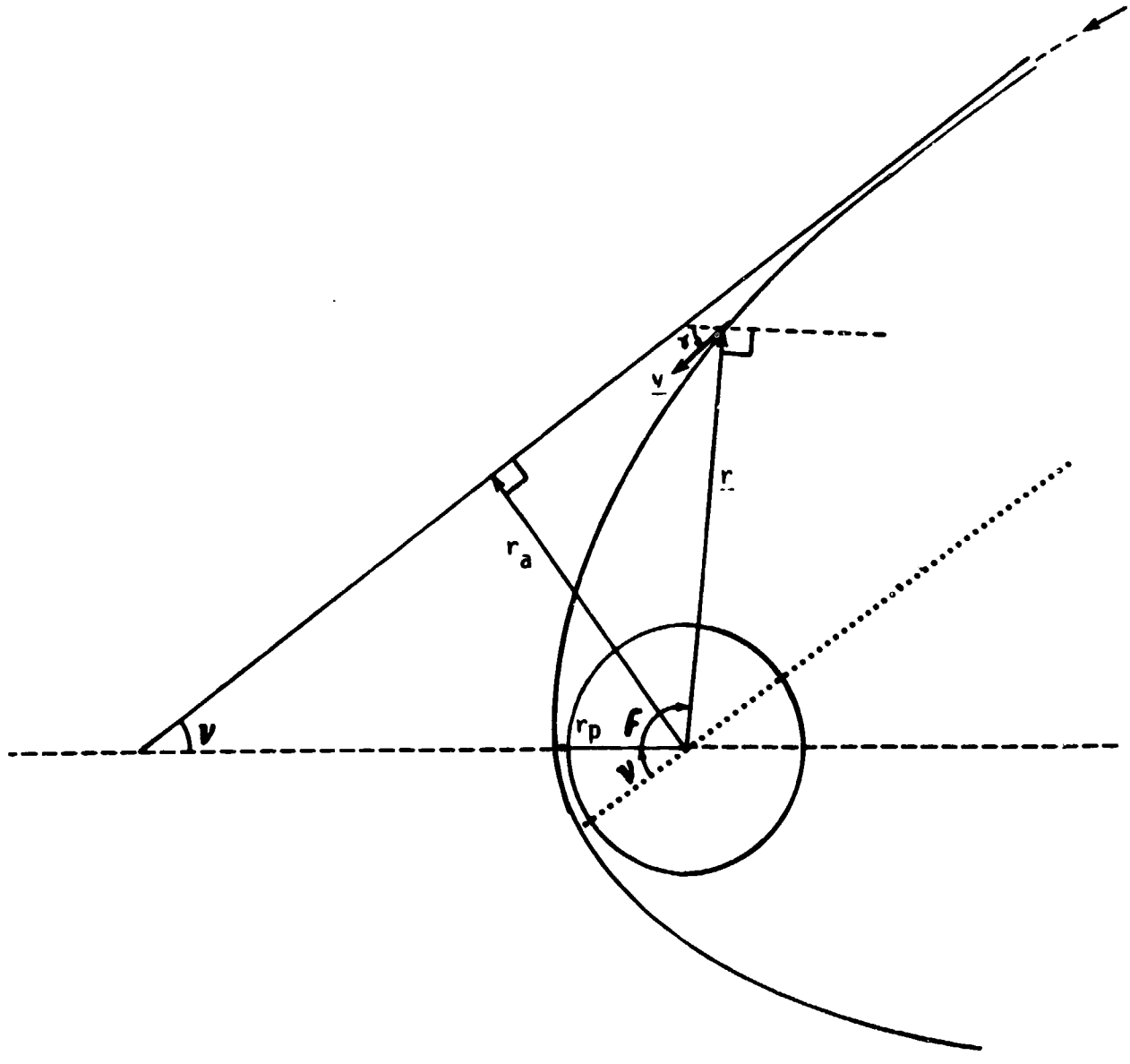

Figure A-1: Hyperbolic Encounter Geometry

$$r_a = r_p \sqrt{1 + 2\mu/r_p\, v_\infty^2} \qquad \text{(A-6)}$$

Equations (A-1) involve, however, atmospheric airmass relative velocity and associated flight path angle, rather than inertial quantities. As

$$\underline{v} = \underline{v}_i - \underline{\Omega} \times \underline{r} \qquad \text{(A-7)}$$

where Ω is the earth's angular velocity, the parameter sets are related by

$$v = v_i \sqrt{1 - 2(\Omega r/v_i)\cos\gamma_i \cos L \sin\psi_i + (\Omega r/v_i)^2 \cos^2 L}$$

$$\sin\gamma = (v_i/v)\sin\gamma_i \qquad \text{(A-8)}$$

with

L = latitude

ψ_i = inertial velocity azimuth from north

The possible combinations of entry latitude and azimuth, however, are constrained by the relation

$$\sin\psi_i = -\cos i/\cos L \qquad \text{(A-9)}$$

where i is the angle of inclination of the orbit to the earth's equatorial plane. Noting, furthermore, that, for hyperbolic orbits, $v_i \gg \Omega r$, then, for all but the steepest values of γ_i, i

$$v \approx v_i(1 + (\Omega r/v_i)\cos\gamma_i \cos i) \qquad \text{(A-10)}$$

The inclination of the orbit is limited from below by the declination of the hyperbolic asymptote, so that the specification of a value of $\cos i$,

and therefore v, is not completely free.

Sample Mars return orbits, as described by $\underline{v}_\infty$, are given in Table A-1.

Table A-1: MSR Sample Orbits

	v_∞ (km/sec)	λ(deg)	δ(deg)
1	3.07	200.02	27.13
2	3.24	232.58	-52.45
3	2.82	314.52	-43.44

where λ is the right ascension and δ the declination. The corresponding atmospheric encounter velocities are computed from Equation (A-4) and Equation (A-10), and given in Table A-2.

Table A-2: MSR Atmospheric Encounter Velocities

	v_i(kms/sec)	v_{max}(kms/sec)*	v_{min}(kms/sec)*
1	11.49216	11.7012	11.27927
2	11.53876	11.6823	11.39341
3	11.42793	11.5987	11.25453

*Note: for $\gamma_i = 0$

A.3 Approximate Analytical Solutions

A number of approximate analytical solutions for the atmospheric entry dynamics have been formulated by various investigators, and have been treated in unified fashion by Loh [3]. First, the relationship between atmospheric density and altitude is written as an exponential

$$\rho = \rho_s \, e^{-h/h_s} \tag{A-11}$$

where

ρ_s = reference (surface) density

h_s = atmospheric scale height

Then, noting that

$$\frac{d\rho}{dt} = -(\rho/h_s)\,\frac{dh}{dt} \tag{A-12}$$

and manipulating Equations (A-1), the following pair of equations is obtained.

$$\frac{d\cos\gamma}{d\rho} = \frac{1}{2}\left(\frac{L}{D}\right)\left(\frac{C_D A}{m}\right)h_s + \frac{\cos\gamma}{\rho}\left(1 - \frac{gr}{v^2}\right)\frac{h_s}{r}$$

$$\frac{d(v^2/gr)}{d\rho} = \frac{2h_s}{r\rho} - \left(\frac{C_D A}{m}\right)\frac{(v^2/gr)}{\sin}\,h_s \tag{A-13}$$

It is then found that

i) The term $\cos\gamma\,(1 - gr/v^2)h_s/r\rho$ is relatively insensitive to variations in γ and ρ along the path.

ii) $2/r\rho \ll (C_DA/m)(v^2/gr)\sin\gamma$

Equations (3-13) can then be approximately solved to yield

$$\cos\gamma - \cos\gamma_0 \approx N(\rho-\rho_0)$$

$$\ell n[v^2/v_0^2] \approx (C_DA/m)h_s(\gamma - \gamma_0)/N \qquad \text{(A-14)}$$

$$N = \frac{1}{2}(L/D)(C_DA/m)h_s + \cos\gamma\,(1 - gr/v^2)h_s/r\rho$$

where ρ_0, v_0, γ_0 are initial conditions. These equations can then be solved to yield two of the variables (e.g., v, γ) as a function of the third.

Furthermore, the above equations can be utilized to obtain the max deceleration and max heating rates for the trajectory. The max deceleration point occurs when

$$\frac{d}{dv}\left(\frac{dv}{dt}\right) \approx \frac{d}{dv}(\rho v^2) = 0 \qquad \text{(A-15)}$$

Utilizing Equations (A-13), the maximum deceleration occurs approximately when

$$(C_DA/m)h_s/\rho = \sin\gamma \qquad \text{(A-16)}$$

This additional relation allows complete solution of Equations (A-14) for ρ, v, δ at the max deceleration point, and by back substitution, the corresponding max deceleration value.

Similarly, the max convective heat rate is obtained when

$$\frac{d}{dv}\left(\frac{dQ_c}{dt}\right) \approx \frac{d}{dv}(\rho^{1/2}\, v^{3.15}) = 0 \qquad \text{(A-17)}$$

A similar procedure as above allows determination of the max heating rate, and the values of the trajectory parameters when it occurs.

A.3.1 Explicit Approximate Solutions - Direct Entry. Further simplifications, reflecting constraints on the character of the entry path, allow an explicit analytical solution to be obtained. Two examples are provided below:

A. Gliding Entry at Small Flight Path Angles

Assuming $\cos\gamma \approx \cos\gamma_o \approx 1$, Equations (A-14) can be simplified to

$$v^2/gr_e \approx 1/[1 + (r_e/2)(L/D)(C_D A/m)\rho]$$

$$\sin\gamma \approx (2h_s/r_e)/(L/D)(v^2/gr_e) \qquad \text{(A-18)}$$

The range, or distance travelled along the path, which, for small angles of inclination, is equal to the horizontal range, is obtained by integrating

$$R = \int dR = \int v dt$$

$$R \approx (r_e/2)(L/D)\ln[(1-v^2/gr_e)/(1-v_o^2/gr_e)] \qquad \text{(A-19)}$$

The vehicle deceleration is given approximately by

$$\frac{dv}{dt} \approx -D \approx -g(1 - v^2/gr_e)/(L/D) \qquad \text{(A-20)}$$

For this trajectory, no peak deceleration is encountered; rather, the deceleration asymptotically approaches the value

$$-\left(\frac{dv}{dt}\right)_{max} = g/(L/D) \qquad \text{(A-21)}$$

The peak convective heat rate is given by

$$\left(\frac{dQ_c}{dt}\right)_{max} \approx \frac{2\sqrt{2}}{3\sqrt{3}} K \sqrt{g/R_N \, B(L/D)} \, (gr_e) \qquad \text{(A-22)}$$

b. Ballistic Entry at Median and Large Flight Path Angles

In this case, the entry path is approximately linear, with

$$\cos\gamma \approx \cos\gamma_o - (C_D A/m) h_s (\rho - \rho_o)/\sin\gamma \qquad \text{(A-23)}$$

$$v^2 \approx v_o^2 \, e$$

The max deceleration is approximately given by

$$\left(\frac{dv}{dt}\right)_{max} \approx -(1/2\, e\, h_s) v_o^2 \sin\gamma_o \qquad \text{(A-24)}$$

and the max convective heating rate by

$$\left(\frac{dQ_c}{dt}\right)_{max} \approx k \sqrt{\sin\gamma_o / 3e \, B \, h_s \, R_N} \; v_o^3 \qquad \text{(A-25)}$$

A.3.2 Explicit Approximate Solutions - Atmospheric Braking. For relatively small variations in γ and ρ throughout the path, the parameter N in Equations (A-14) can be assumed to be approximately constant. A good representative value is stated by Loh to be that which obtains at the minimum path altitude (i.e., $\gamma = 0$).

$$\cos\gamma \approx 1 + N_m(\rho - \rho_m)$$

$$v^2 \approx v_m^2 \, e^{-(C_D A/m) h_s \gamma / N_m} \qquad \text{(A-26)}$$

where the m subscript indicates values at the minimum path altitude. In these equations, negative flight path angles pertain to the path prior to the $\gamma = 0$ point, with positive values thereafter.

Furthermore, from this representation of the path, the atmospheric exit conditions can be derived as

$$\cos\gamma_E \approx 1 - N_m \rho_m \Rightarrow \gamma_E \approx -\gamma_o$$
$$v_E^2 \approx v_m^2 \, e^{(C_D A/m) h_s \gamma_o / N_m} \Rightarrow v_E \approx v_m^2 / v_o \qquad \text{(A-27)}$$